A STUDY OF
THE SAL NEUTRON DETECTOR EFFICIENCY
USING PHOTODISINTEGRATION OF THE DEUTERON

A Thesis

Submitted to the College of Graduate Studies and Research

in Partial Fulfillment of the Requirements

for the Degree of Master of Science

in the

Department of Physics and

Engineering Physics

University of Saskatchewan

by

Jiansen Lu

Saskatoon, Saskatchewan

CANADA

In presenting this thesis in partial fulfillment of the requirements for a Postgraduate degree from the University of Saskatchewan, the author agrees that the Libraries of this University may make it freely available for inspection. The author further agrees that permission for copying of this thesis in any manner, in whole or in part, for scholarly purposes may be granted by the professor or professors who supervised the thesis work or, in their absence, by the Head of the Department or the Dean of the College in which the thesis work was done. It is understood that any copying or publication or use of this thesis or parts thereof for financial gain shall not be allowed without the author's written permission. It is also understood that due recognition shall be given to the author and to the University of Saskatchewan in any scholarly use which may be made of any material in the thesis.

Requests for permission to copy or make other use of material in this thesis in whole or part should be addressed to:

Head of the Department of Physics and Engineering Physics
University of Saskatchewan
Saskatoon, Saskatchewan S7N 0W0

Abstract

This thesis uses the detector simulation software package GEANT to simulate the SAL neutron detector efficiency, and compares the results to data from the SAL experiment 003. The simulation was designed to mimic the experiment 003 experimental setup. Experiment 003 used the Saskatchewan-Alberta Large Acceptance Detector (SALAD) to detect protons from photodisintegration of the Deuteron and used the SAL neutron detector to detect the neutrons from this reaction. The outgoing neutron energy and direction can be calculated from the tagged photon energy and the outgoing proton angle by using two-body kinematics. The neutron detector efficiency can be obtained from comparing the number of neutrons detected by the neutron detector and the number of neutrons impinging on the detector. A good agreement was obtained between the simulation results and the data from experiment 003, thus giving us confidence that the simulation code is correct. The SAL neutron detector efficiency could then be determined from the simulation and is presented as a function of the incident neutron energy. The neutron detector intrinsic efficiency will be applied to the approved SAL proposal experiment 043: photo-proton production from ^{12}C.

Acknowledgements

Many thanks go to my supervisor Dr. Rob Pywell. Without his guidance and kindness, I cannot imagine I can finish this thesis.

Many thanks go to Dr. D.M. Skopik, the director of Saskatchewan Accelerator Lab. He gives me a very good opportunity to study and do the experiment in SAL and this changes part of my life.

I also would like to thank Dr. Norm Kolb and Post Doctor Fellow Farida Adimi and Ph.D student Ken Garrow. They help me a lot in my experiment and study.

I also want to thank my fellow graduate students Dave Lee Hornidge, Terry Pilling, Carsten Muller, Shahram Alavian and Shi Fang who keep my life fun.

I also want to thank all the SAL staff's kindness and friendship.

Finally I must thank my wife Hui Xu. With her encouragement, I continue to stay in my science and research career.

Contents

List of Figures

List of Tables

Glossary

ADC	Analog to Digital Converter
CAMAC	Computer Automated Measurement and Control Standard
CERN	European Organization for Nuclear Research
ECS	Energy Compression System
GEANT	Detector simulation software developed at CERN
LINAC	LINear Accelerator
LUCID	Data acquisition and analysis software developed at SAL
MLU	Multiplicity Logic Unit
PAW	Physics Analysis Workstation
PID	Particle IDentification
PSR	Pulse Stretcher Ring
SALAD	Saskatchewan Alberta Large Acceptance Detector
SAL	Saskatchewan Accelerator Laboratory
STU	SAL Tagger Unit
TDC	Time-to-Digital Converter
UNIX	Trademark of UNIX system laboratory

Chapter 1

Introduction

1.1 Photonuclear Reactions

The structure of the atom was known after Rutherford's α-scattering experiments in 1909. From the angular distribution of α particles scattered from a target, Rutherford and his colleagues suggested that an atom has a diameter of about 10^{-10} m and near the centre of the atom is a nucleus, which contains 99.9% of the mass of the atom, and has a diameter of about 10^{-15} m. Later researchers showed that a nucleus consists of protons and neutrons and the interaction between them is via the strong force mediated by the exchange of pions. Protons and neutrons in turn are made of quarks. The nucleon-nucleon interaction is complicated and has distance-dependent, spin-dependent, velocity-dependent and non-central terms. The study of the nucleon-nucleon force will help us understand the nuclear structure, the strong interaction and quark models.

Photon beams have been a useful probe in studying nuclear structure because photons only interact with the nuclear constituents by the electromagnetic interaction which is described by quantum electrodynamics (QED) and is well understood. A photon can couple to the nuclear charge, current and magnetic moment. The strength of the electromagnetic interaction is much smaller than the nuclear force, so the photon coupling to the nuclear current can be separated from the nuclear force. High duty factor accelerators make the measurements of correlations between reaction products from photonuclear reactions possible. A photon tagging facility allows the energy of a photon initiating a nuclear reaction to be precisely measured.

At low photon energies (< 50 MeV), photon absorption may be understood in terms of a photon being absorbed by an individual nucleon. When the incident photon

energy is about 150 MeV, the mechanisms for photon absorption by a nucleus may be understood in terms of a photo-mesonic mechanism and a quasi-deuteron mechanism. The quasi-deuteron mechanism is the dominant mechanism in this energy range. In the simple quasi-deuteron mechanism, a photon is absorbed on a neutron-proton pair in a nucleus and the residual nucleus acts as a spectator.

The (γ, pn) reaction process can be described by the following diagram:

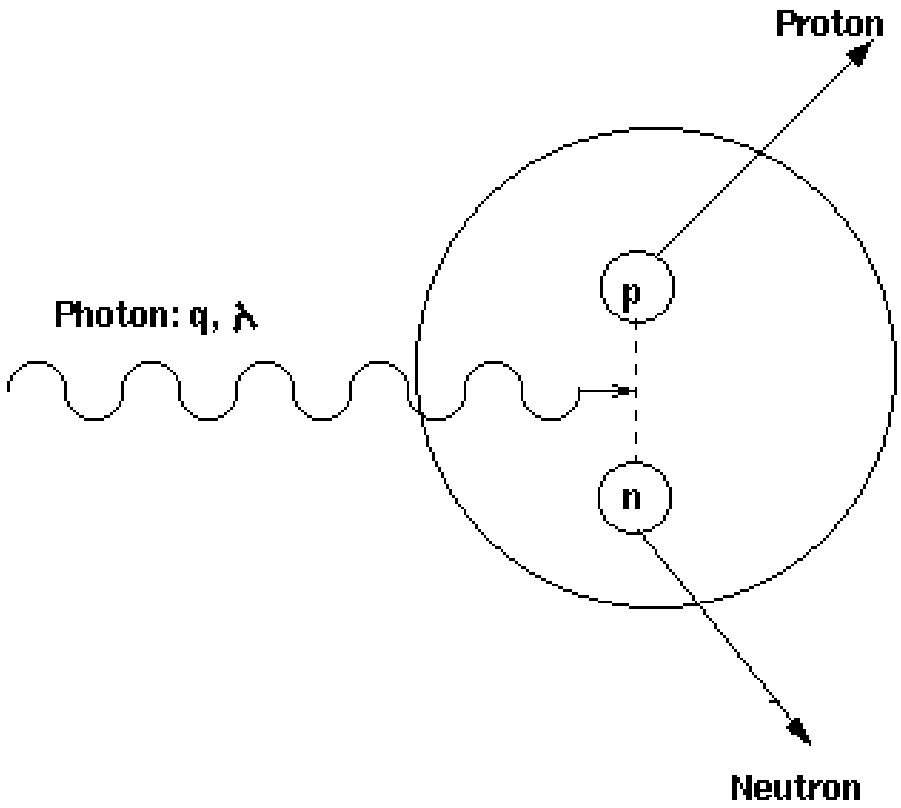

Figure 1.1: Photodisintegration diagram for(γ, pn) reaction process.

The (γ, pn) reaction cross section is proportional to the squared Feynman amplitude M. The Feynman amplitude M of photonuclear reactions can be written as follows:

$$M = \int d\overrightarrow{r}\, e^{i\overrightarrow{q}\cdot\overrightarrow{r}} < \Psi_f | \overrightarrow{J}(\overrightarrow{r}) \cdot \overrightarrow{\epsilon_\lambda} | \Psi_i > \tag{1.1}$$

Here Ψ_i is the nucleus initial state wavefunction, Ψ_f is the nucleus final state wavefunction, $\overrightarrow{\epsilon_\lambda}$ is the photon polarization vector and $\overrightarrow{J}(\overrightarrow{r})$ is the nuclear current operator. $\overrightarrow{q}$ is the momentum transferred to the target by the absorbed photon.

In the simple quasi-deuteron mechanism, the total nuclear photodisintegration cross section can be simply written as

$$\sigma = L\frac{NZ}{A}\sigma_d \tag{1.2}$$

Here L is the Levinger constant which accounts for differences in nuclear density. $\frac{LNZ}{A}$ can be understood as the probability to find a quasideuteron pair in the ground state nucleus. N is the neutron number in a nucleus, Z is the proton number in a nucleus, A is the nucleus atomic number and σ_d is the Deuteron photodisintegration cross section.

The measurement of the energies and angles of neutrons and protons emitted during photodisintegration of a nucleus may be used to reconstruct the recoil momentum distribution of the residual nucleus. The residual nucleus energy state can then be determined. This may be compared to model predictions. The (γ, pn) reaction cross section can also be obtained for comparison to theoretical predictions. The need to measure the outgoing neutron energy and angle leads to the need for SAL to build a neutron detector.

1.2 The SAL Neutron Detector Efficiency

1.2.1 The SAL Neutron Detector

The neutron detector is made from bars of plastic known as scintillators. The use of scintillators can be traced back to the early years of nuclear physics. When a ZnS scintillator was struck by an α particle in Rutherford's α scattering experiment, it emitted a light which could be seen by the naked eye. Nowadays, people use photomultipliers to collect the light.

The SAL neutron detector E scintillators are made of ten thick bars of Bicron

BC-408 plastic scintillator. In front of these bars are ten thin bars of Bicron BC-412 plastic scintillator known as veto scintillators. These allow the rejection of charged particles as will be explained later. The E scintillators and the veto scintillators are connected to photomultipliers by lucite light guides. The photomultipliers convert a light signal to a pulse of electric current. A scintillator's light output is nearly proportional to the particle energy deposited in the scintillator. Bicron scintillators are composed of hydrogen and carbon atoms. When a neutron passes through the plastic scintillator, it may interact with a hydrogen nucleus and transfer part of its energy to a recoiling proton which excites the electrons in the scintillator molecules. The molecules soon decay and emit light. The decay time for this light pulse for BC-408 is 2.1 ns, and for BC-412 it is 3.3 ns. The combination of BC-408 and BC-412 scintillators can be used to detect γ rays, fast neutrons and charged particles. For slow neutrons, a detector which contains Boron, like BF_3 gas, may be used.

1.2.2 The SAL Neutron Detector Efficiency

The SAL neutron detector efficiency was studied for determining the (γ, pn) reaction cross section.

The neutron detector efficiency may be described by two quantities: absolute detection efficiency and intrinsic detection efficiency. The intrinsic detection efficiency is more widely used.

$$Absolute\ efficiency = \frac{neutrons\ counted}{neutrons\ emitted\ by\ a\ source} \tag{1.3}$$

$$Intrinsic\ efficiency = \frac{neutrons\ counted}{neutrons\ incident\ on\ a\ detector} \tag{1.4}$$

$$Geometrical\ efficiency = \frac{neutrons\ incident\ on\ a\ detector}{neutrons\ emitted\ by\ a\ source} \tag{1.5}$$

$$Absolute\ efficiency = Intrinsic\ efficiency\ *\ Geometrical\ efficiency \quad (1.6)$$

The *geometrical efficiency* of a detector only depends on the detector's geometry and the relative position between the detector and the source. The intrinsic efficiency of a detector depends on the incident particle's type and energy, and what kind of the detector is used.

The SAL neutron detector intrinsic efficiency may be written as:

$$\epsilon_t = \epsilon_c(1 - e^{-dN\sigma}) \quad (1.7)$$

Here ϵ_c is the efficiency correction shown in equation 1.9, d is the neutron path length in the detector, N is the number density of the target nucleus in the detector, and σ is the neutron interaction cross section with the detector nuclei.

Because neutrons can interact with both carbon and hydrogen nuclei in the SAL neutron detector, so the total interaction cross section σ can be written as

$$N\sigma = N_H\sigma_H + N_C\sigma_C \quad (1.8)$$

Here N_H is the number density of hydrogen nuclei in the detector, σ_H is the neutron interaction cross section with hydrogen nuclei, N_C is the number density of carbon nuclei in the detector and σ_C is the neutron interaction cross section with carbon nuclei.

Because the light output of a neutron detector mainly comes from recoiling protons due to a neutron interaction with a hydrogen nucleus, rather than from a neutron interaction with a massive carbon nucleus, the efficiency correction ϵ_c is given by

$$\epsilon_c = \frac{N_H\sigma_H}{N_H\sigma_H + N_C\sigma_C}. \quad (1.9)$$

The equation 1.7 only gives an approximation for the efficiency calculation. A more detailed calculation can be obtained by a simulation which uses the software GEANT. GEANT, which was developed at the European Organization for Nuclear

Research (CERN), is a very good tool to simulate a detector response, even when the detector is complex. The simulation program is divided into the following eight parts: common blocks, GEANT initialization, detector setup, event generation, hit data structure, detector response, tracking and data output.

Five processes of neutron interaction with a detector were considered in this simulation. These are: elastic scattering, inelastic scattering, neutron capture, charged particle emission and fission.

This simulation program uses the PATCHY code management system and the program was written in FORTRAN 77. The histograms in the simulation were displayed using the Physics Analysis Workstation (PAW) software. PATCHY and PAW were also developed at CERN. In July 1997, the simulation program was upgraded to the GEANT 97 version which does not use PATCHY code management system.

Data from experiment 003, a deuteron photodisintegration experiment, which was done at the Saskatchewan Accelerator Lab in June, 1995, was used to experimentally obtain the SAL neutron detector efficiency and test the simulation code.

In experiment 003, SALAD (the Saskatchewan-Alberta Large Acceptance Detector) was used to detect the protons from photodisintegration of a Deuteron and the SAL neutron detector was used to detect the neutrons. The outgoing neutron energy and direction can be calculated from the known photon energy and the outgoing proton angle by using two-body kinematics. Some of the outgoing neutrons may interact with the SAL neutron detector. The detected neutron's outgoing angle can be calculated from the time difference between signals reaching the left end and the right end of the SAL neutron detector bars. Their energy can be calculated from the time of flight of the neutron from the target to the detector. The neutron detector efficiency can be obtained from comparing the number of neutrons detected by the detector and the number of neutrons impinging on the detector. A good agreement was shown between the simulation results and the data from experiment 003. The neutron detector intrinsic efficiency will be applied to the approved SAL proposal experiment 043: photo-proton production from ^{12}C. This experiment will use SALAD and the neutron detector, i.e. the same configuration as in the simulation.

The experiment 003 setup will be presented in Chapter 2. The experiment 003 data analysis will be presented in Chapter 3. The simulation process will be described in Chapter 4. The comparison between the simulation results and data from experiment 003 will be discussed in Chapter 5.

Chapter 2

Experiment 003 Set-up

2.1 The Experiment

Experiment 003 was designed to measure the reaction products from the photodisintegration of a Deuteron, i.e. $^2H(\gamma, pn)$. Data from experiment 003 were used to obtain the SAL neutron detector efficiency for comparison with the simulation results. The experiment 003 setup is shown in Figure 2.1. The outgoing proton from photodisintegration of a Deuteron was detected by SALAD which is shown in Figure 2.1 as a cylinder. With the known tagged photon energy and the outgoing proton angle measured from the wire chambers in SALAD, the outgoing neutron energy and angle was obtained by using two-body kinematics. Then the number of neutrons impinging on the neutron detector was known. This can be compared to the number of neutrons detected by the neutron detector, which is shown in Figure 2.1 as a wall of bars, to determine the detector efficiency.

2.2 Tagged Photon Beam

Experiment 003 was done at the Saskatchewan Accelerator Laboratory (SAL) in June, 1995. The SAL layout is shown in Figure 2.2.

SAL produces a high duty factor and high energy electron beam by a combination of a 300 MeV linear accelerator (LINAC), an energy compression system (ECS) and a pulse stretcher ring (PSR). The photon tagging facility at SAL is used for nuclear photodisintegration experiments. Six five-meter long microwave accelerating sections are the main parts of the linear accelerator. 2856 MHz microwaves, which are amplified by klystrons, transfer their energy to electrons as they travel along the accelerating sections. The electron energy may be increased to 300 MeV after 6 ac-

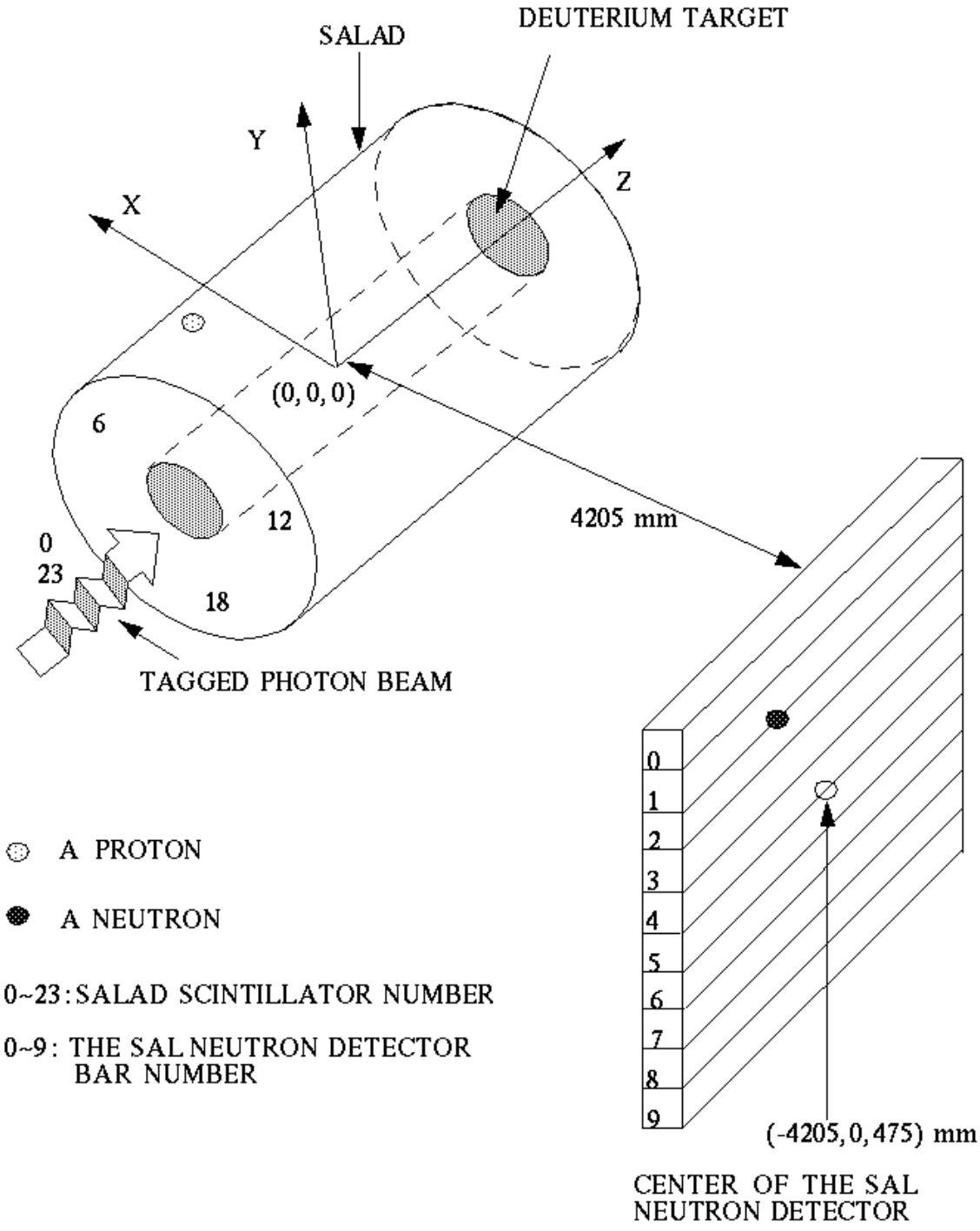

Figure 2.1: Exp003 setup and coordinates

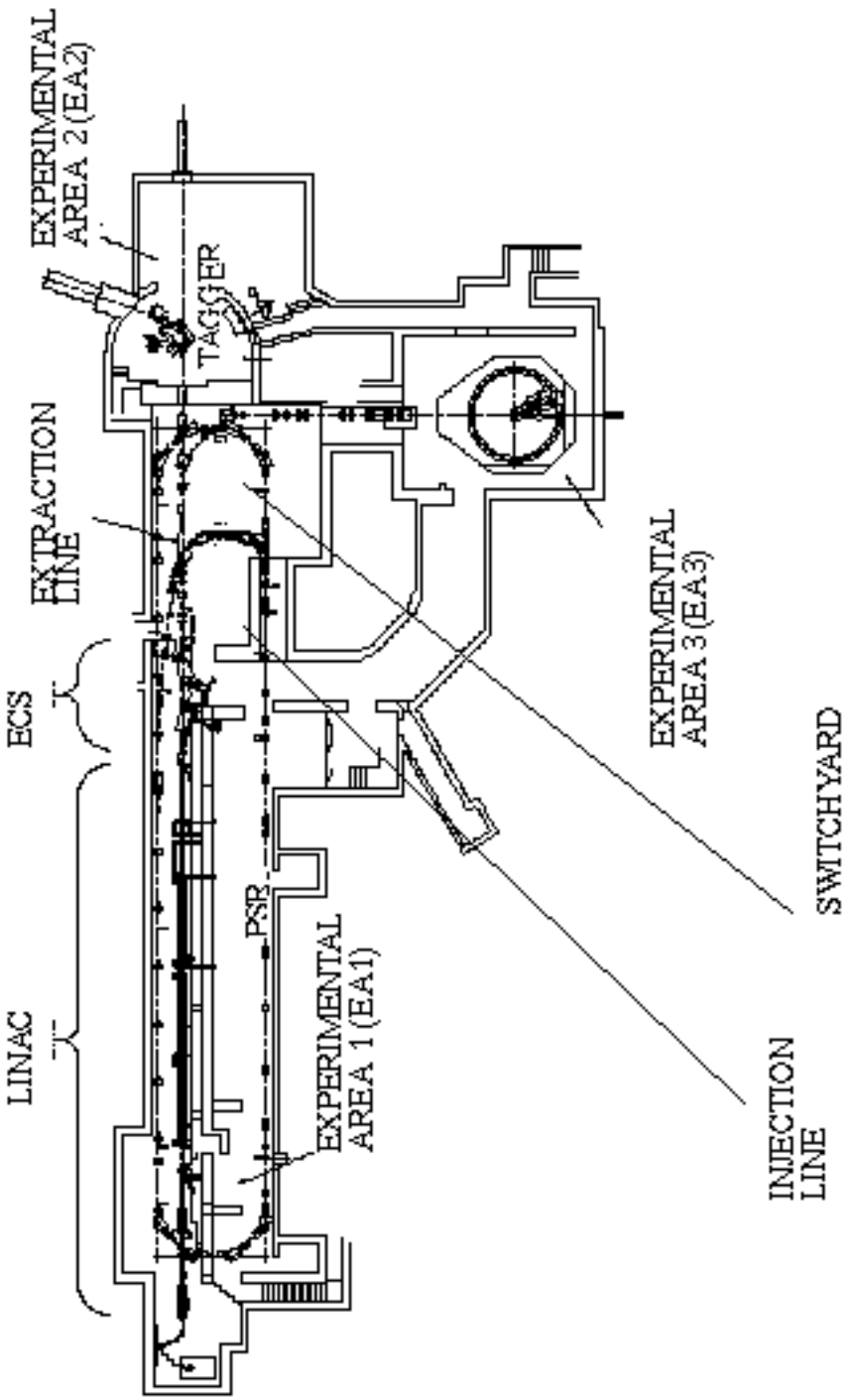

Figure 2.2: The SAL layout

celerating sections. The repeat frequency of microwave pulses is usually 180 Hz and the length of the electron pulses is about 400 ns. Thus the duty factor of electrons from the LINAC is less than 0.1%. The energy compression system reduces the energy spread of the electron beam from the linear accelerator by a factor of about 10. This is necessary for injection into the pulse stretcher ring. The pulse stretcher ring transforms a low duty factor electron beam to a high duty factor electron beam.

The electron beam coming from the pulse stretcher ring hits an aluminum radiator and produces a narrow, forward-pointing cone of bremsstrahlung photons. The post-bremsstrahlung electrons are momentum analyzed by a photon tagging spectrometer which has a 62-channel focal plane. The detection energy resolution of this residual electron beam is approximately 1%. The difference between the incident electron energy and the measured energy of the post-bremsstrahlung electron gives the energy of the bremsstrahlung photon. The bremsstrahlung photon beam is collimated by two 12.6-cm-long lead collimators. This defines the size of the photon beam at the target. The first collimator has a diameter of 15 mm; the other one has a diameter of 20 mm.

In this experiment, the average electron beam energy was 252.3 MeV, the average duty factor was about 58% and tagger central momentum was set to 136.5 MeV/c which resulted in tagged photons with an energy range from 73.41 MeV to 142.50 MeV. The tagged photon energy distribution, which is related to the hit pattern spectrum on the focal plane detector, is shown in Figure 2.3. A photon tagger energy calibration related to tagger channels is shown in Appendix B.

2.3 The Target

The target gas was deuterium. The pressure of the target gas was 7 atm and the temperature of the target gas was 300 K. The target cell was a 2.37 m long, 50.5 mm in radius Mylar lined carbon fiber tube. Both ends of the target cell were fitted to

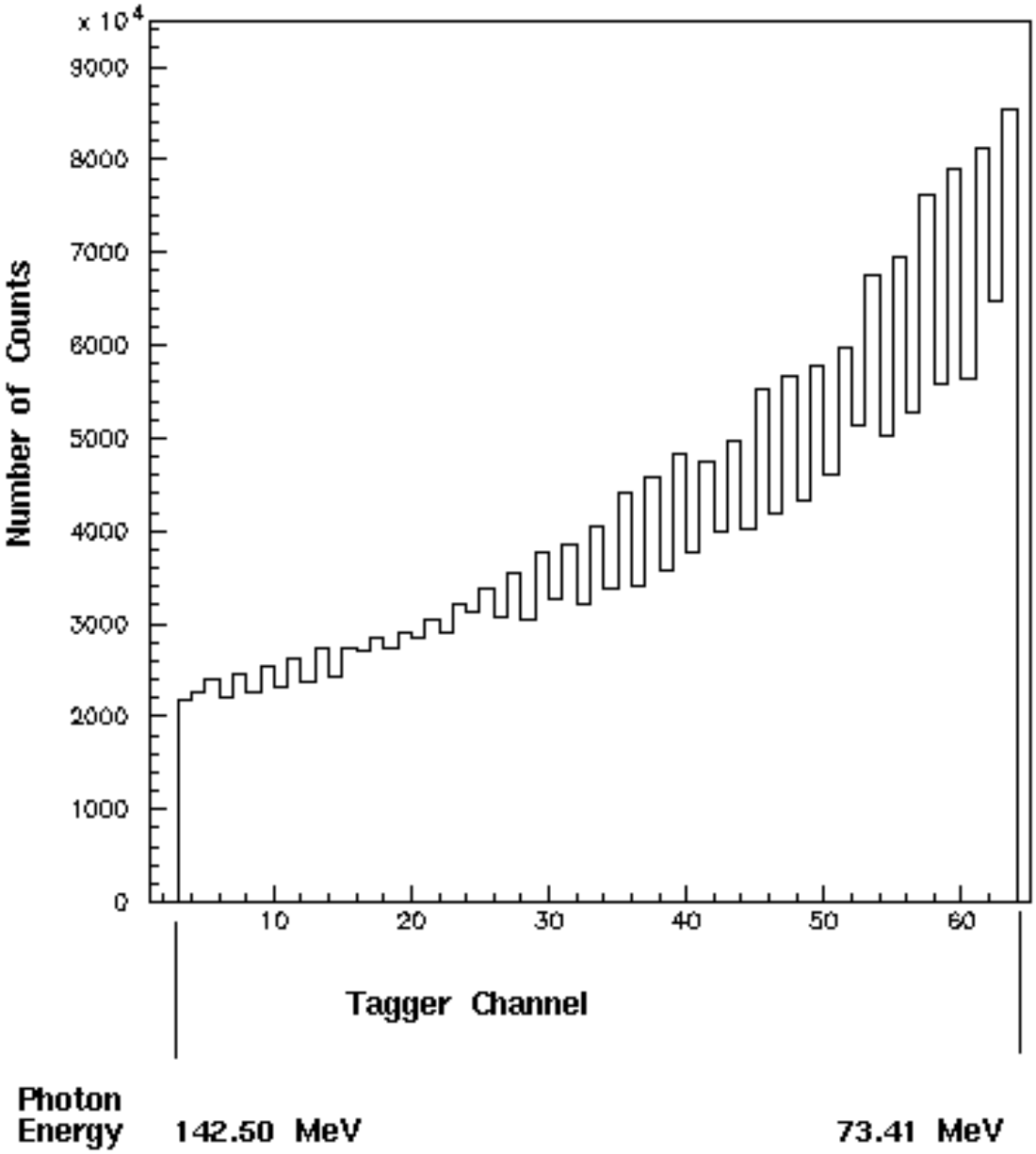

Figure 2.3: The tagged photon beam energy distribution in Exp003

an aluminum tube.

2.4 The Detector

The detectors used in this experiment are SALAD and the SAL neutron detector. SALAD was used to detect the protons. The neutron detector was used to detect the neutrons. SALAD and the SAL neutron detector will be introduced in the following sections.

2.4.1 SALAD

The geometry of SALAD is shown in Figure 2.4. A detailed description of SALAD is given in P.P. Langill's M.Sc. thesis [12] and E.B. Cairns's paper [3].

Wire chambers and plastics scintillators are the main parts of SALAD. The wire chambers were filled with 70% isobutane gas (C_4H_{10}) and 30% Argon by volume so that wire chambers could work in self-quenching-streamer (SQS) mode. A high voltage was maintained between anode wire and walls of wire chamber cells. Ions produced by the passage of a charged particle through the gas were accelerated toward the wire, ionizing more atoms on the way. Argon gas produced a high charge gain due to the gas multiplication. Isobutane gas operated to limit the charge avalanche and kept wire chambers working stably. The charge was deposited on the wires and was collected at the upstream and downstream ends of the wires. The z position of the hit along the wires is nearly proportional to the difference in charge collected between two ends of the wires relative to the total charge.

In this experiment, the first three wire chambers worked on high voltages -3.8 kV (anode wire relative to cell walls) and the fourth wire chamber worked on -3.9 kV so that a maximum wire chamber efficiency could be achieved. The relative position of anode wires and wire chambers is shown in Figure 2.5. Wire chamber leakage current (the current drawn from the high voltage supply) should be kept below 10 μA. Unfortunately, the third wire chamber could not hold full high voltage; it tripped off

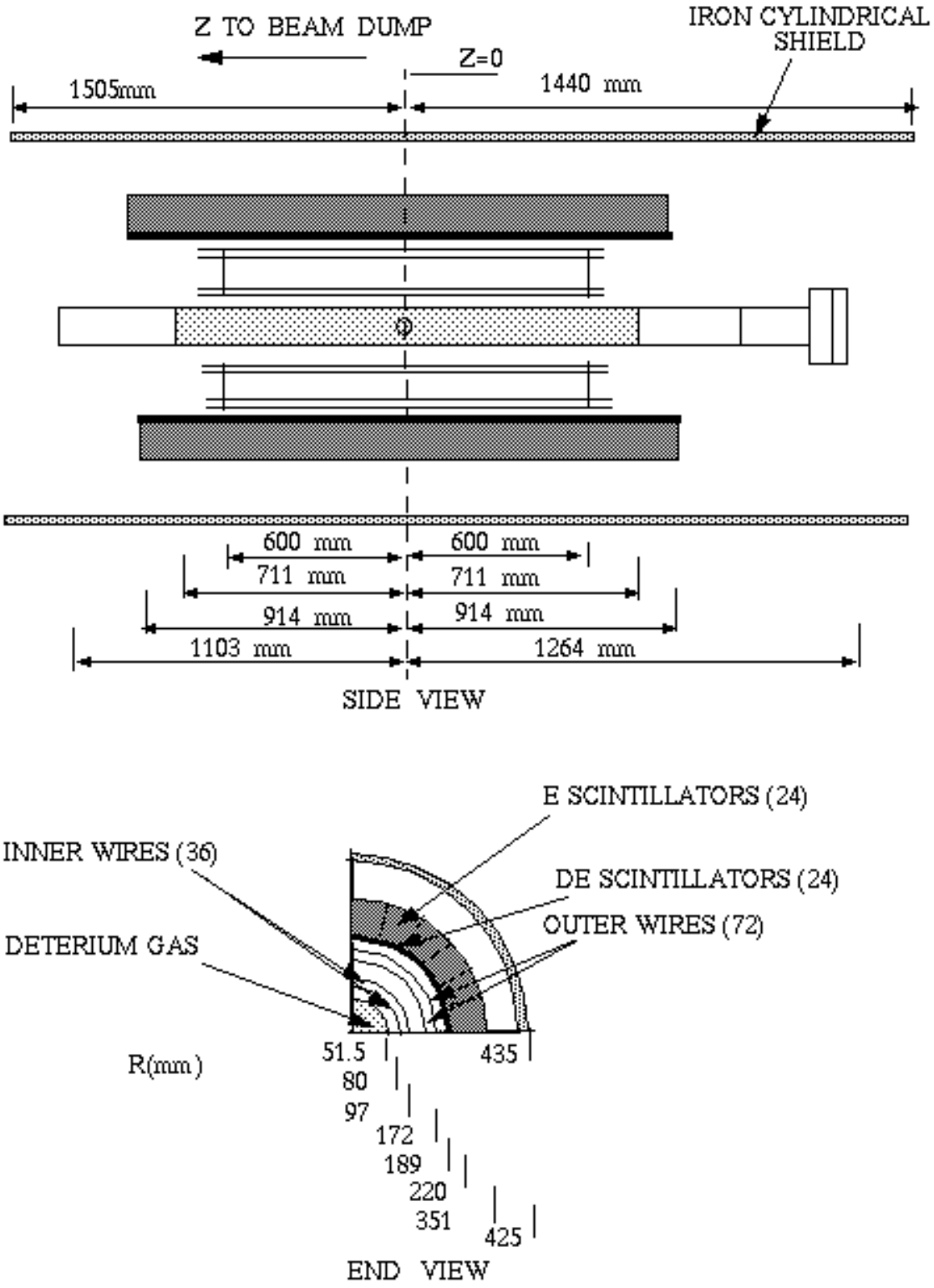

Figure 2.4: A schematic of SALAD

at -3.2 kV. The third wire chamber had to be given up, but this did not seriously influence tracking a charged particle.

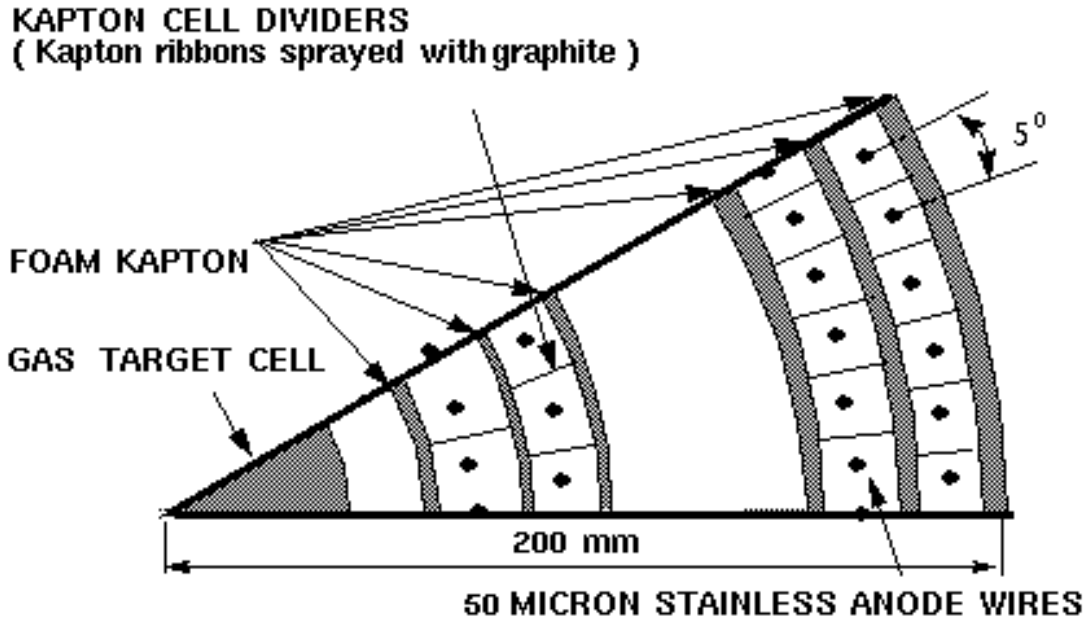

Figure 2.5: An end view schematic of the wire chambers

SALAD E scintillators have a thickness of 127 mm and a length of 1829 mm. SALAD ΔE scintillators have a thickness of 3.2 mm and a length of 1803 mm. The SALAD E scintillators are made of Bicron BC-408 plastic scintillator. The SALAD ΔE scintillators are made of Bicron BC-412 plastic scintillator. The SALAD ΔE-E scintillator pairs may be used to distinguish pions, protons and deuterons. Electron backgrounds and neutrons can also be identified by using the SALAD ΔE-E telescopes.

2.4.2 The SAL Neutron Detector

The outline of the SAL neutron detector is shown in Figure 2.6.

The SAL neutron detector consists of ten bars of Bicron BC-408 plastic scintillators. Another ten bars of Bicron BC-412 plastic scintillators work as the veto detector. Each bar in the SAL neutron detector and the veto detector has the same length –

1500 mm and the same width – 150 mm. The thickness of the SAL neutron detector is 76 mm and the thickness of the veto detector is 3 mm. The veto detector is used to distinguish neutrons from charged particles, because neutrons do not deposit energy in the veto detector, while charged particles do. A detailed description of the SAL neutron detector may be found in Keith Helgason's M.Sc. thesis [9].

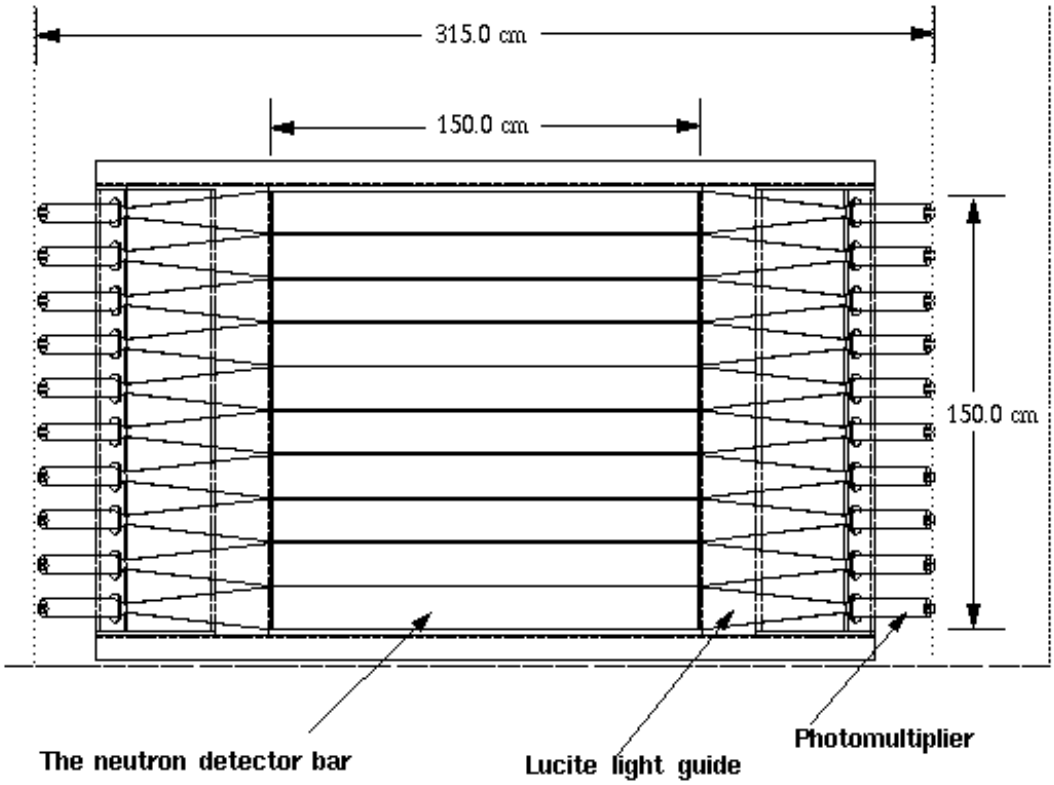

Figure 2.6: A schematic of the SAL neutron detector

Both ends of each neutron detector bar were connected to photomultipliers by lucite light guides for coupling. The SAL neutron detector light guides are 205 mm long. One end of each light guide was coupled to the SAL neutron detector. The other end was coupled to a photomultiplier 125 mms in diameter. The veto detector light guides have a length of 612 mm. One end of each veto detector light guide was coupled to the veto detector. The other end was connected to a photomultiplier 50 mms in diameter.

2.5 Data Acquisition Electronics

The data acquisition system in experiment 003 may be classified as either hardware or software. Hardware components are: tagger CAMAC modules, SALAD FASTBUS modules and CAMAC modules, the SAL neutron detector CAMAC modules, a front end processor, a SUN UNIX workstation, tape drive and 8 mm tapes. Each 8 mm tape can store 2 Gbytes of data. The data acquisition software, LUCID, was developed at the Saskatchewan Accelerator Laboratory and was used to acquire and analyze data. In LUCID, the READER component was used to take data from CAMAC online or to take data from tapes offline, the LOOKER component was used to analyze the data and the WRITER component was used to store the data. The data acquisition system is shown in Figure 2.7.

The SALAD trigger logic is shown in Figure 2.8. Some of the basic electronics used in experiment 003 are described below:

ADC : Analog-to-Digital Converter. The LeCroy CAMAC Model 2249A ADC was used for the neutron detector data acquisition. The LeCroy FASTBUS Model 1882 charge sensitive ADC was used for SALAD data acquisition. The signals which came from the SALAD E and ΔE photomultipliers were imported to The LeCroy Model 1882 ADC. These ADC values were analyzed by a computer and were used to determine the proton energy later. The ADC values from the wires in wire chambers were used to determine the proton hit position along the wires.

TDC : Time-to-Digital Converter. The LeCroy FASTBUS Model 1875 TDC was used for SALAD data acquisition. The LeCroy CAMAC Model 2229 TDC was used for the neutron detector data acquisition. This neutron detector TDC was used to determine the neutron hit position along the neutron detector and to determine the neutron time of flight. For the SALAD TDC and the neutron detector TDC, the start signals came from the SALAD master gate and the stop signal came from the photomultipliers. Before doing experiment 003, a

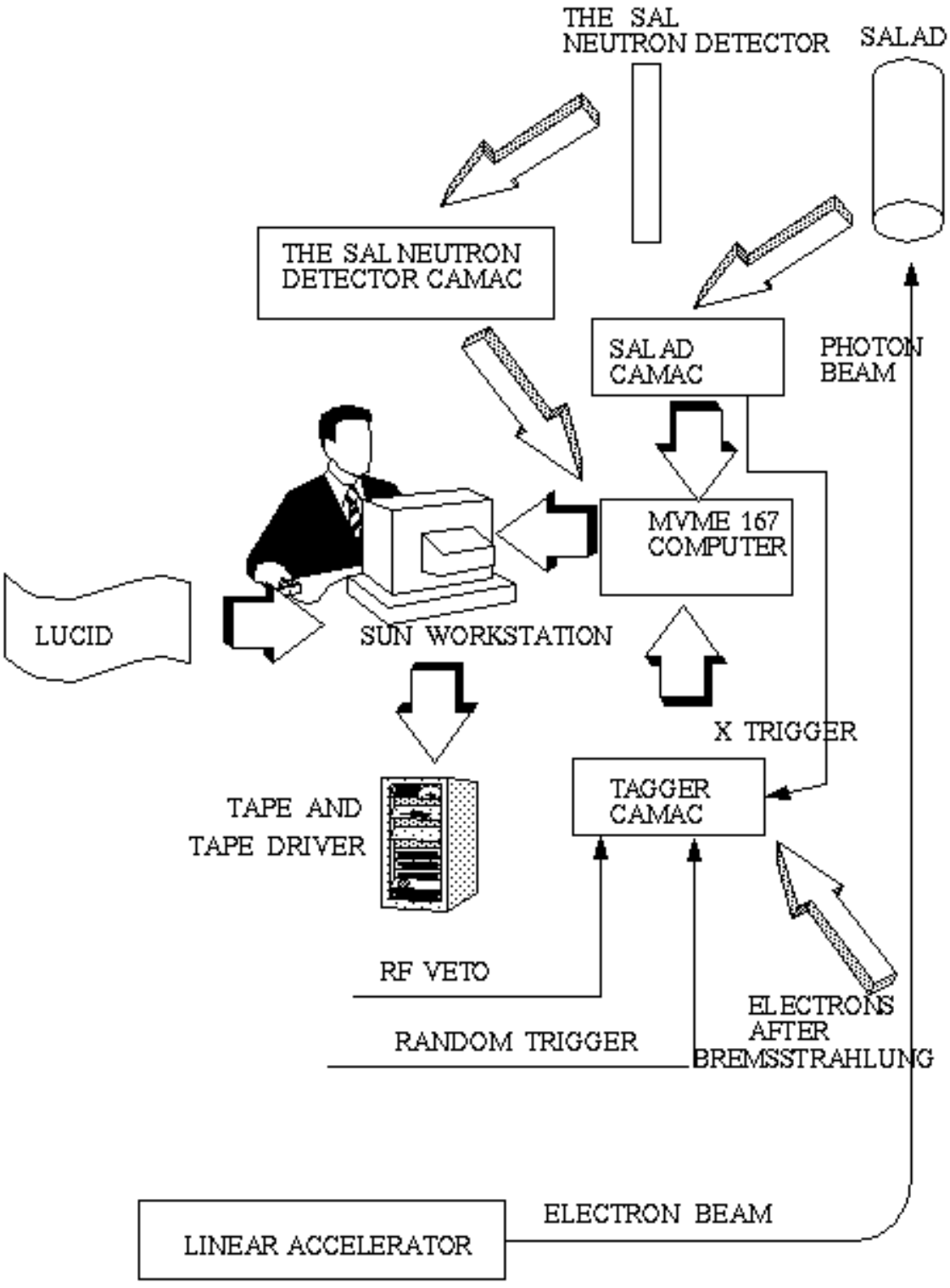

Figure 2.7: Experiment 003 data acquisition system

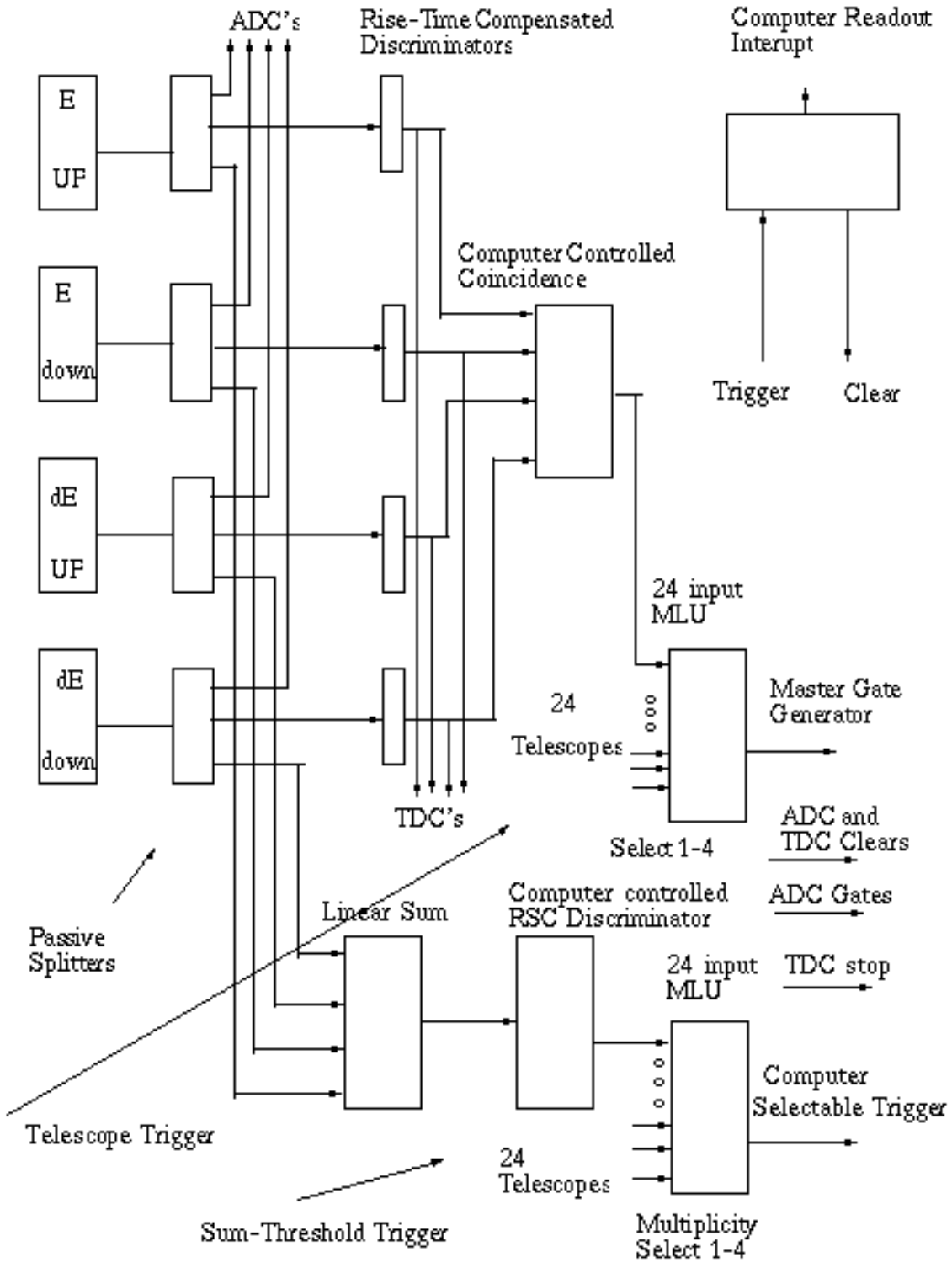

Figure 2.8: A schematic of the SALAD trigger logic

suitable delay was added to ensure that the start signal is always a little ahead of the stop signal.

MLU : Multiplicity Logic Unit. Two trigger circuits were used in the experiment. In the first trigger circuit, i.e. the scintillator trigger circuit, the four output signals from the upstream ΔE-E pair and the downstream ΔE-E pair were sent to a 4-fold coincidence unit. Any combination of these four output signals above threshold may be required for a trigger. In the second trigger circuit, i.e. the sum-threshold trigger circuit, the four output signals from the upstream ΔE-E pair and the downstream ΔE-E pair were summed in a linear Fan in/Fan out module and the output was compared with a discriminator setting.

In either the scintillator trigger circuit or the sum-threshold circuit, the outputs from the 24 ΔE-E coincidences were sent to a 24 input multiplicity logic unit (MLU) which defined the number of SALAD ΔE-E scintillator telescopes required to trigger the experiment, i.e. multiplicity. The multiplicity in this experiment can be selected as 1, 2, 3 or 4. In a calibration run to determine the gain of scintillators using cosmic rays, a scintillator trigger was selected, and the multiplicity was set 2 because two telescopes were needed to define a cosmic muon track. In a SALAD data run, a sum-threshold trigger was selected to reject electron background online, and the multiplicity was set 1 because only one telescope was needed to detect a proton in SALAD in this experiment.

Chapter 3

Data Analysis

3.1 Introduction

The SAL neutron detector efficiency data analysis flow chart is shown in Figure 3.1. The data analysis will be discussed in three steps: checking the calibration parameters, skimming the data and calculating the detector efficiency.

3.2 Detector Calibrations

3.2.1 A Position Calibration in the SAL Neutron Detector

A neutron energy can be calculated from its velocity. The velocity of the neutron which impinged on the neutron detector can be calculated by using the distance from the target to the neutron detector divided by the neutron time of flight from the target to the detector. The neutron hit position along the neutron detector had to be obtained for calculating the distance from the target to the neutron detector.

The neutron hit position along the neutron detector is proportional to the time difference between the light reaching the left end and right end of the detector bars, which is equal to the TDC reading difference between the left end and right end of the detector bars. The relation between the neutron hit position along the detector and this TDC reading difference can be written as

$$z = a + b * diff \tag{3.1}$$

Here z is the neutron hit position along the neutron detector, *diff* is TDC reading difference between two ends of the detector bar, and a and b are constants which can be obtained by using cosmic ray muons. During the position calibration using the

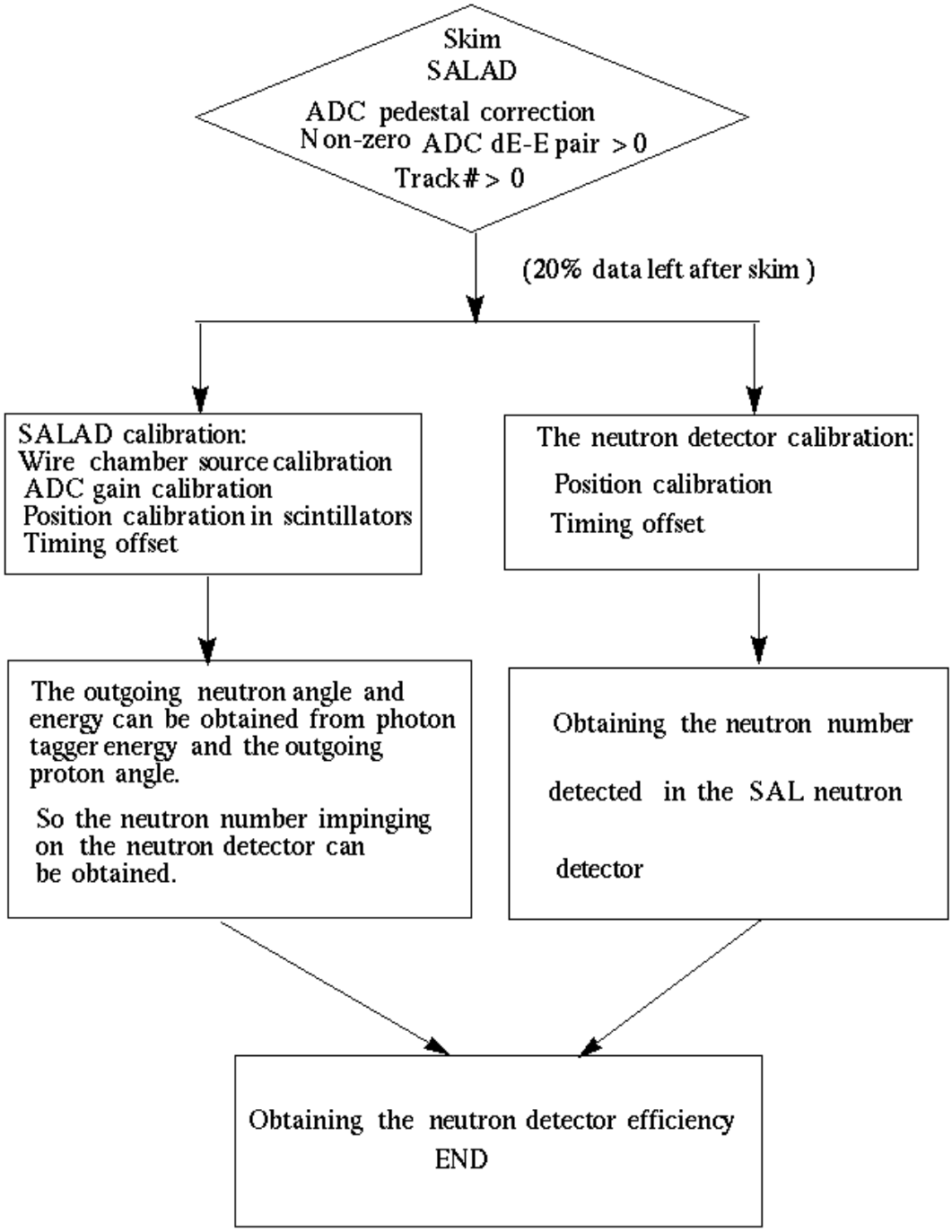

Figure 3.1: The flow chart of Exp003 data analysis

cosmic muons, z is understood as the cosmic muon hit position along the neutron detector.

To determine the cosmic muon hit position along the neutron detector, six paddles, which were made of plastic scintillators, were set between the neutron detector bars and were classified as two groups: upper paddles and lower paddles. The upper paddle and lower paddle positions are shown in Figure 3.2. Coincidences between the upper paddles and lower paddles gave the cosmic muon tracks in the neutron detector.

The trigger electronics for a position calibration are shown in Figure 3.3. The paddles were connected to a LeCroy model 4448 coincidence register to define the trigger patterns. The coincidences between the upper paddles and lower paddles gave 9 trigger patterns. For example, the coincidence between paddle #1 and paddle #4 in Figure 3.2 gave the trigger pattern 1. In this trigger pattern, the cosmic ray muon tracks in each neutron detector bar can be calculated from the position of paddle #1 and paddle #4. A two-dimensional histogram for the cosmic muon track position in each neutron detector bar and the TDC reading difference between the left end and right end of each neutron detector bar can be obtained. The two dimensional histogram for the 4th neutron detector bar is shown in Figure 3.4.

The fourth neutron detector bar position calibration coefficient can be obtained from this two dimensional histogram by using a linear least-squares fit. This meana that if n points of experiment data z and $diff$ are known and $\overline{z}$ is defined as the average of z and $\overline{diff}$ is defined as the average of $diff$, the position calibration coefficient b and a in equation 3.1 will be estimated as follows:

$$b = \frac{\sum_{i=1}^{n}(z_i - \overline{z})(diff_i - \overline{diff})}{\sum_{i=1}^{n}(diff_i - \overline{diff})^2} \tag{3.2}$$

$$a = \overline{z} - b * \overline{diff}. \tag{3.3}$$

The fourth neutron detector bar position calibration coefficients are shown in

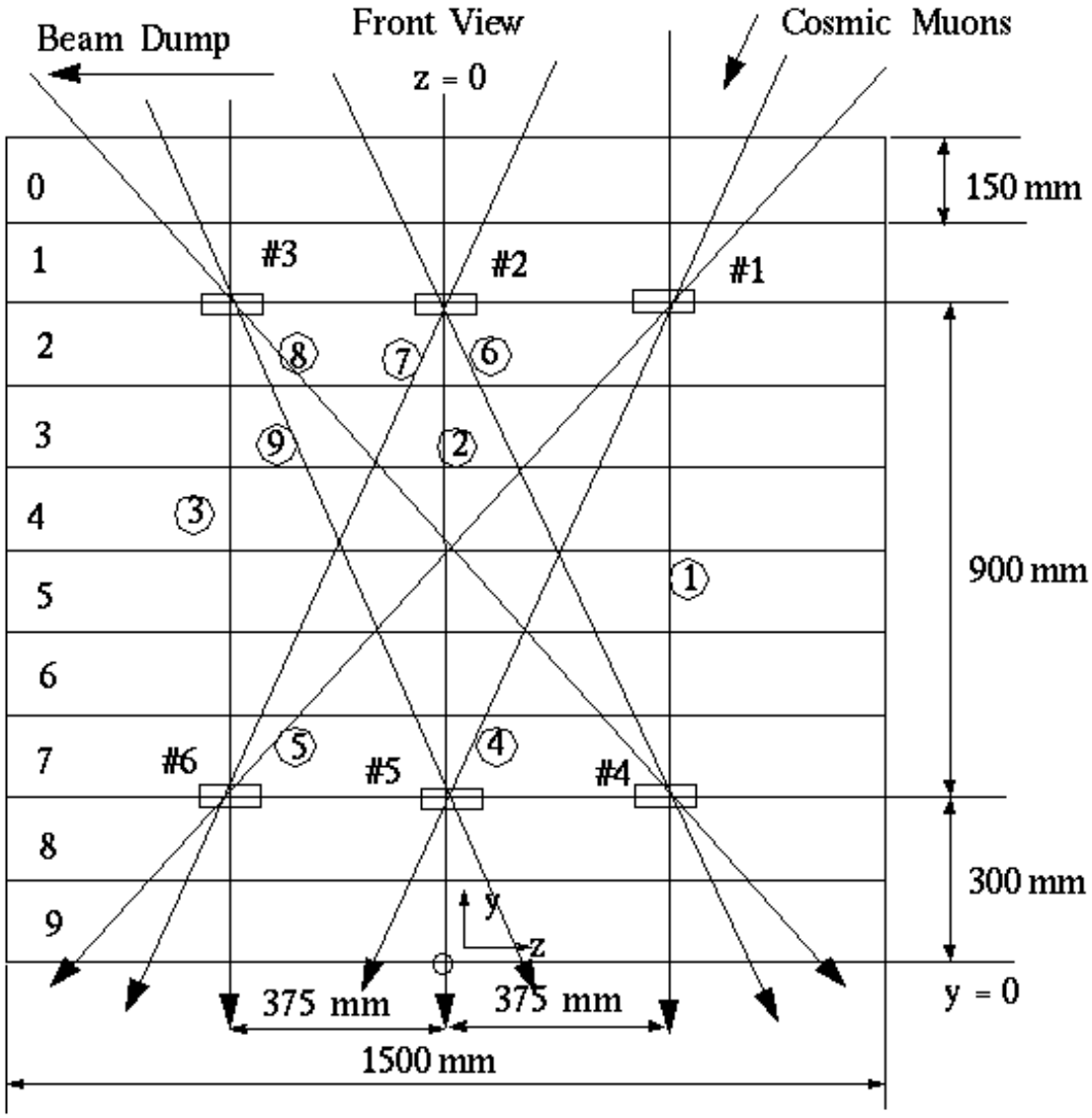

Figure 3.2: Paddle setup for the neutron detector position calibration

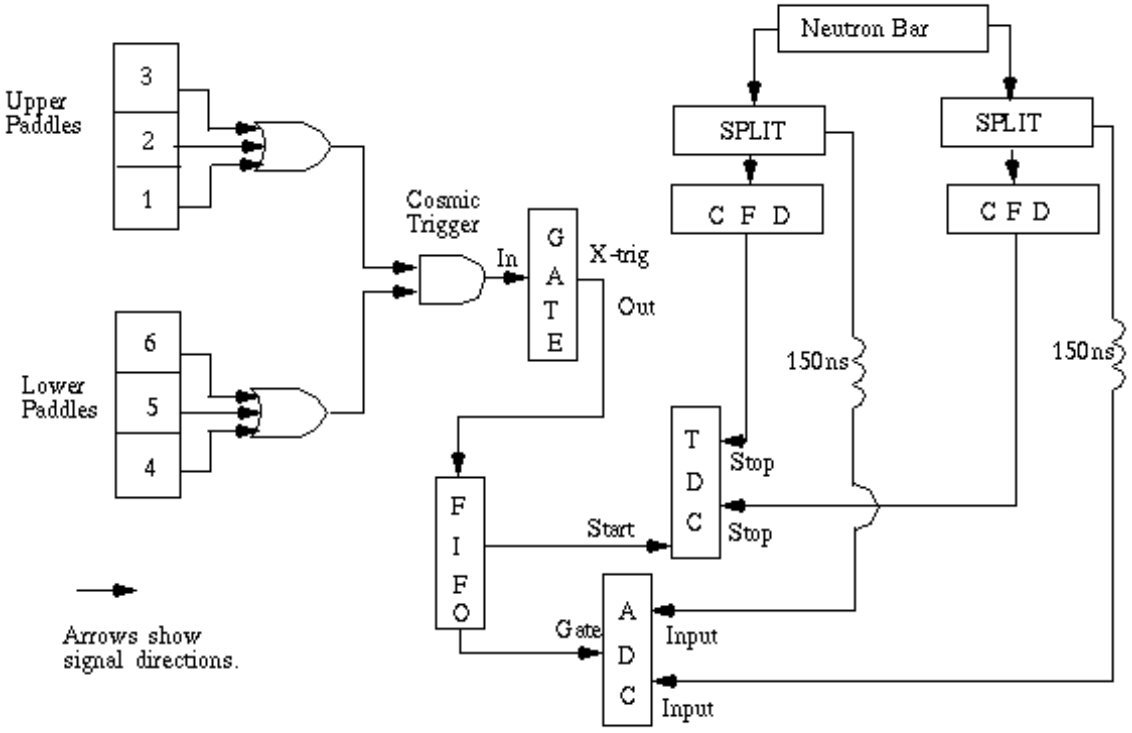

Figure 3.3: The neutron detector position calibration circuit diagram

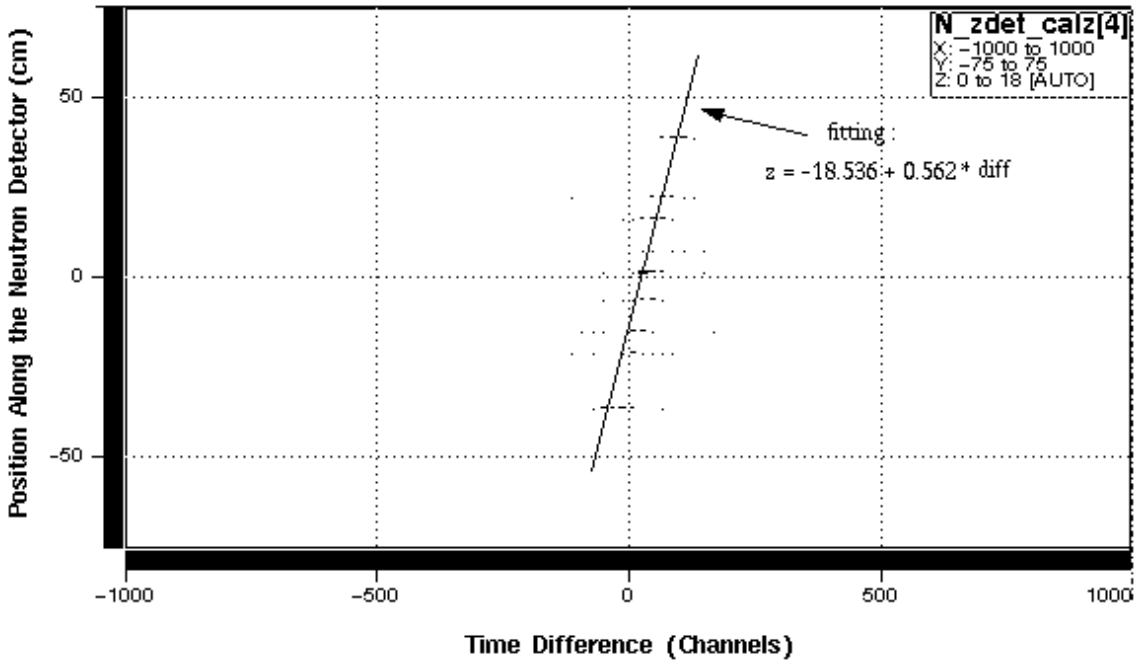

Figure 3.4: A 2-D histogram for the cosmic muon track position in the 4th neutron detector bar and the TDC reading (100 ps/channel) difference between the left end and right end of the 4th neutron detector bar

Figure 3.4. The other bar position calibration coefficients can be obtained by using the same process as for the fourth bar.

3.2.2 Timing Offsets in SALAD and the SAL Neutron Detector

For determining the time of flight of a neutron, timing offsets for SALAD and the SAL neutron detector must be determined. The calculation of time of flight of a neutron is detailed in Appendix A.

The neutron time of flight can be obtained from the equation A.22 in Appendix A as follows:

$$f_n = t_n + f_i - t_i + K_i^p - K_n^p. \tag{3.4}$$

In this equation f_n is the neutron time of flight from the target to the n^{th} detector bar when a neutron hits the n^{th} detector bar, t_n is the TDC reading average between the left end and right end of the n^{th} neutron detector bar, f_i is the proton time of flight from the target to the i^{th} SALAD E scintillator, t_i is the TDC reading average between upstream and downstream of the i^{th} SALAD E scintillator, K_i^p is the timing offset for the i^{th} SALAD E scintillator and K_n^p is the timing offset for the n^{th} neutron detector bar.

For obtaining the timing offset K_i^p, a special timing paddle, which was made of plastic scintillator, was put 470 mm under the SALAD iron cylinder and 1400 mm from the downstream edge of the cylinder. The timing offset K_i^p can be obtained from the equation A.14 in Appendix A as follows:

$$K_i^p = t_i^s + f_c - P_s. \tag{3.5}$$

In this equation t_i^s is the TDC reading average between the upstream and downstream of the i^{th} SALAD E scintillator and f_c is the cosmic muon time of flight from the i^{th} SALAD E scintillator to the timing paddle. The cosmic muon's velocity is close to

the speed of light, so f_c can be obtained from the cosmic muon flight distance from the i^{th} SALAD E scintillator to the timing paddle. P_s is the paddle TDC reading in the SALAD TDC. The timing offsets K_i^p for each SALAD E scintillator can be obtained from the prompt peak in histograms of K_i^p. A Histogram of timing offset K_i^p for the 8th SALAD E scintillator is shown in Figure 3.5.

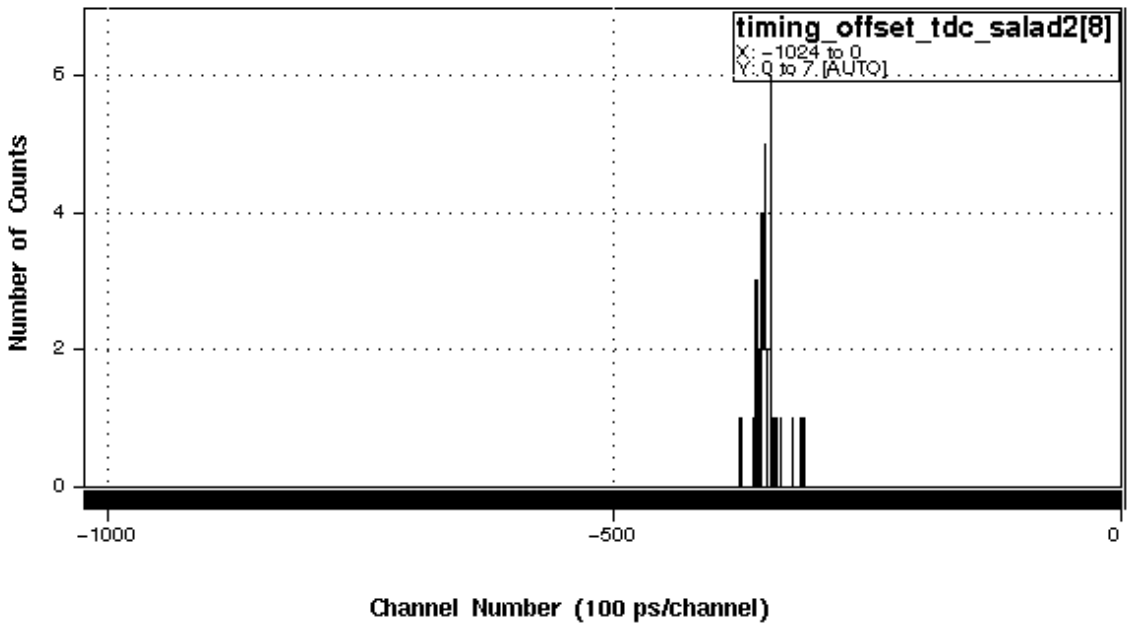

Figure 3.5: A histogram of timing offset K_i^p for the 8th SALAD E scintillator

For obtaining the timing offset K_n^p, the same timing paddle was put under the center of the 10th neutron detector bar. The timing offset K_n^p can be obtained from the equation A.20 in Appendix A as follows:

$$K_n^p = t_n^n + f_q - P_n. \tag{3.6}$$

In this equation t_n^n is the TDC reading average between the left side and right side of the n^{th} neutron detector bar and f_q is the cosmic muon time of flight from the n^{th} neutron detector bar to the timing paddle. f_q can be calculated by using the cosmic muon flight distance from the n^{th} neutron detector bar to the timing paddle. P_n is the paddle TDC reading in SALAD TDC. The timing offsets K_n^p for each neutron

detector bar can be obtained from the prompt peak in histograms of K_n^p. A histogram of timing offset K_n^p for the 3th SALAD neutron bar is shown in Figure 3.6.

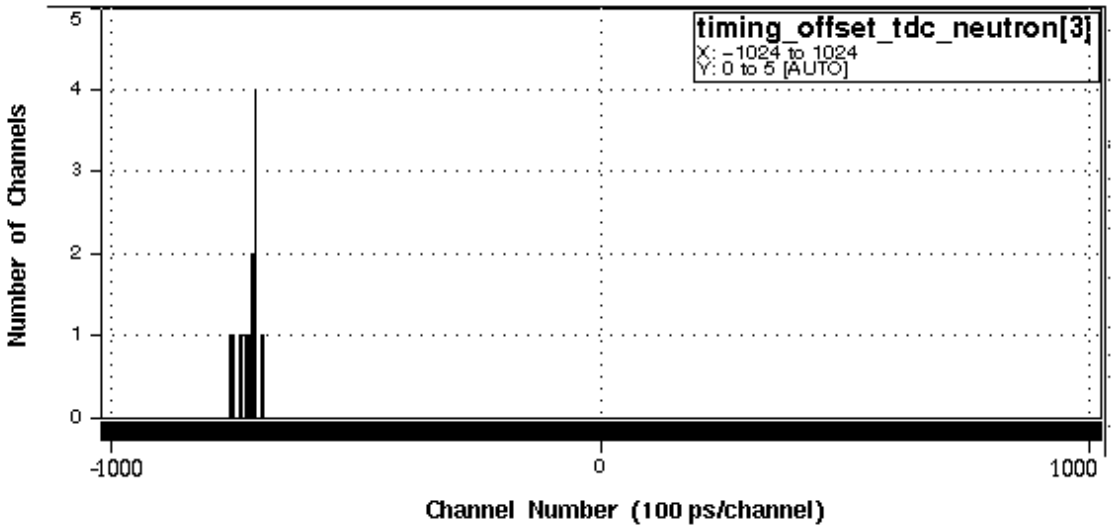

Figure 3.6: A histogram of timing offset K_n^p for the 3th neutron detector bar

3.2.3 Position Calibration for the SALAD Wire Chambers

The wire chambers operated in self-quenching-streamer (SQS) mode. The region of the charge deposited on the wires was localized. The charge deposited on the wires divided into two parts and propagated along to the upstream and downstream ends of the wires. The position along the wires is nearly proportional to ΔQ, the difference between the charge collected at the two ends of the wires relative to the total charge.

$$\Delta Q = \frac{(Q_{up} - Q_{down})}{(Q_{up} + Q_{down})} \tag{3.7}$$

Here Q_{up} is the charge collected at the upstream end of the wires, Q_{down} is the charge collected at the downstream end of the wires and the position Z along the wires can be calculated from the ΔQ.

$$Z = A_0 + A_1 \Delta Q + A_2 \Delta Q^2 \tag{3.8}$$

Here A_0, A_1 and A_2 are constants which can be obtained from runs with radioactive sources near the wire chambers. Two ^{55}Fe sources were mounted in the space between the inner chambers and the outer chambers. One of these sources illuminated the inner chambers and the other illuminated the outer chambers.

These two sources were remotely controlled by a computer and can be positioned at any point along the z-axis of the wire chambers and can be moved to any angle ϕ around the axis of SALAD.

Data were taken with the sources at seven different z positions: 0, -150, 150, -300, 300, -450 and 450 mm. At each z position, the sources were rotated around the axis of SALAD in 5^0 steps.

3.2.4 SALAD Scintillator Gain Calibration

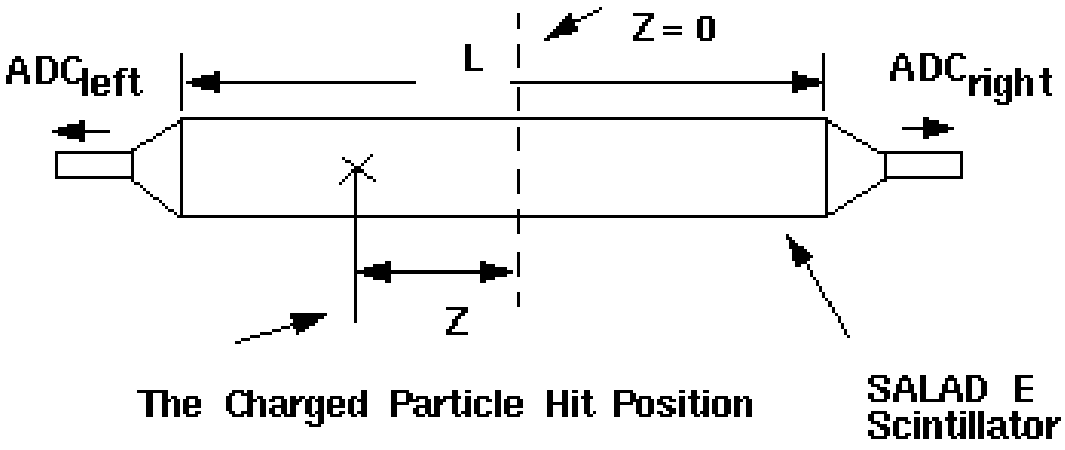

Figure 3.7: A schematic for a charged particle hitting a SALAD E scintillator

When a charged particle hits a SALAD E scintillator as shown in Figure 3.7, the number of scintillator photons produced by the charged particle is proportional to the energy E_0 which the charged particle deposits in the E scintillator. The ADC outputs from the left side and right side of the E scintillator are related to the charged

particle's hit position and the amount of energy it deposited.

$$ADC_{left} = C_1 E_0 e^{\frac{-Z}{\lambda}} \tag{3.9}$$

$$ADC_{right} = C_2 E_0 e^{\frac{-(L-Z)}{\lambda}} \tag{3.10}$$

Here λ is the attenuation length for photons travelling down the scintillator, E_0 is the amount of energy the charge particle deposited in the scintillator, C_1 and C_2 are constants that depend on the photomultiplier and ADC gains, L is the SALAD E scintillator total length and Z is the charged particle's hit position along the scintillator. The following equation can be obtained by cancelling Z in equation 3.9 and equation 3.10.

$$E_0 = \sqrt{\frac{ADC_{left} ADC_{right}}{C_1 C_2 e^{\frac{-L}{\lambda}}}} \tag{3.11}$$

$$= \frac{\sqrt{ADC_{left} ADC_{right}}}{G} \tag{3.12}$$

$$G = \sqrt{C_1 C_2 e^{\frac{-L}{\lambda}}} \tag{3.13}$$

The gain, G, may be determined by using cosmic muons. A cosmic ray muon is at minimum ionizing and deposits energy a rate of 2.08 MeV/cm in the scintillators. The amount of energy deposited in a scintillator can be calculated from this deposited rate times the path length of the cosmic ray travel through the scintillator, which can be determined from the track direction found using the wire chambers. The gain, G, can be calculated from the following equation.

$$G = \frac{\sqrt{ADC_{left} ADC_{right}}}{E_0} \tag{3.14}$$

3.3 Data Skimming

The data were skimmed so that they could be analyzed more efficiently. Skimming is a process where obvious background events are removed from the data set. The first skim reduced the data by about 20%. First, ADC pedestals were corrected. Pedestal is the ADC output without an analog signal input. Pedestals were measured and then were subtracted from the ADC value during readout. To determine whether pedestals were changing during the experiment, they were read every 10000 SALAD events. This frequency can also be changed during the experiment. The pedestals read during the experiment sometimes varied a little from the pedestals subtracted during data taking. While skimming the data, the following correction was done:

$$ADC_{corrected} = ADC_{original} - Pedestal_{new} + Pedestal_{old} \tag{3.15}$$

Where $ADC_{original}$ was automatically reduced by $Pedestal_{old}$ during the experiment, that means:

$$ADC_{original} = ADC_{measured} - Pedestal_{old}. \tag{3.16}$$

The ADC pedestal should be almost stable during an experiment. Small changes in the pedestals were caused mainly by offset voltage drifts and temperature changes in ADCs.

Since we required a proton in SALAD, the skimming also rejected events in which there was not at least one ΔE-E pair present in the 24 SALAD scintillator telescopes. Skimming also rejected events in which there was not at least one track found in SALAD wire chambers. A track was constructed in SALAD wire chambers by at least one hit in the outer chambers and at least one hit in the inner chambers.

3.4 Data Analysis

3.4.1 A Proton Event Analysis in SALAD

The outgoing proton energy from the photodisintegration of a Deuteron can be calculated from the tagged photon energy and the outgoing proton direction measured in wire chambers. The measurement of the photon energy required that the proton be measured in coincidence with the corresponding post-bremsstrahlung electron.

The tagger TDC spectrum in this experiment is shown in Figure 3.8. The tagger TDC start signal came from the x trigger, which was the trigger from SALAD satisfying a sum-threshold and non-zero ΔE-E telescope requirement. The tagger TDC stop signal came from the tagger focal plane in which the post-bremsstrahlung electrons were detected. The events from the prompt peak in Figure 3.8 are good tagged events, but they include a fair amount of random coincidences. The flat part in the graph is a background of random coincidences between unrelated electrons and x triggers. A good proton event in SALAD should require a true coincidence; that is 474< tagger TDC < 676. At the same time, the random coincidences in this region had to be subtracted.

The random background used for subtraction was estimated from the range 798< tagger TDC < 1000. The events from the ΔT_{good} region in Figure 3.8 were good tagged events. The events from the ΔT_{rand} region in Figure 3.8 were random events. ΔT_{rand} was set the same as ΔT_{good}. Therefore the number of true tagged events can be obtained from the number of good tagged events in the ΔT_{good} region in Figure 3.8 by subtracting the number of random events in the ΔT_{rand} region in Figure 3.8.

The particle identification (PID) process for identifying a proton in SALAD is introduced as follows. When a charged particle passed through a given material, the stopping power approximation for this charged particle is given by the Bethe-Bloch formula [13]

$$\frac{-dE}{dx} = \frac{bZ^2[\ln(a\beta^2\gamma^2) - \beta^2]}{\beta^2}. \tag{3.17}$$

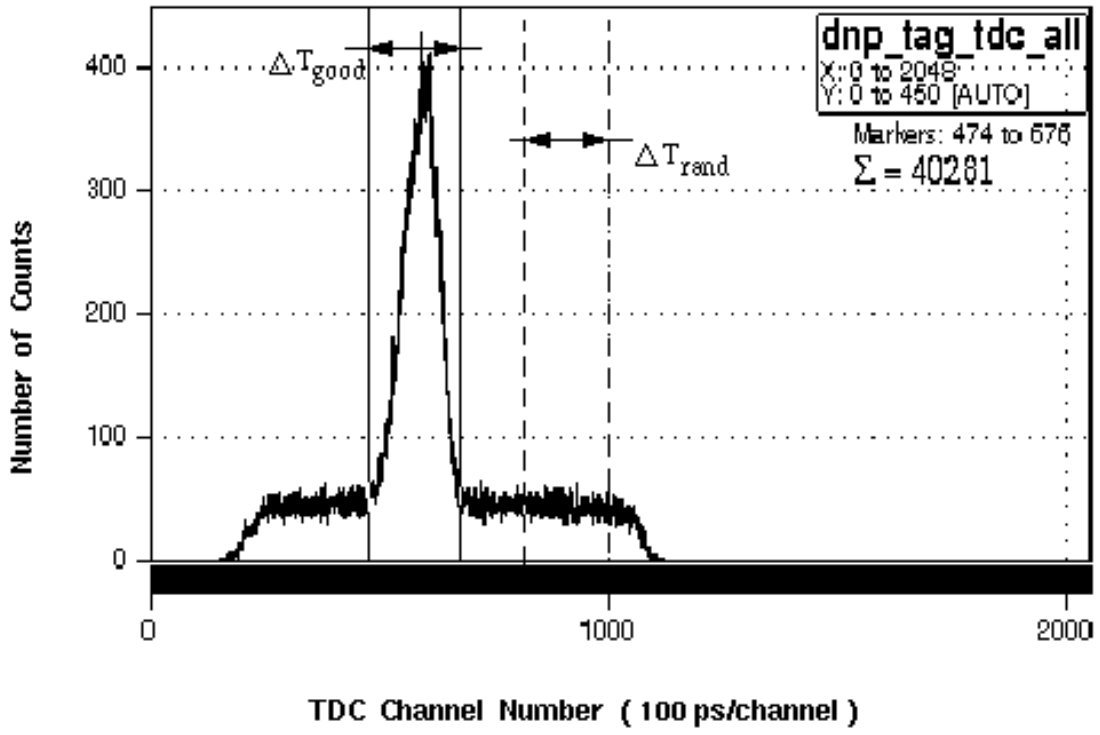

Figure 3.8: Tagger TDC spectrum

In the equation $\frac{dE}{dx}$ is the charged particle energy lost per unit length and b and a are constants for a given material. β and γ is given as follows:

$$\beta = \frac{v}{c} \tag{3.18}$$

Here v is the charged particle velocity and c is the speed of light.

$$\gamma = \frac{1}{\sqrt{(1-\beta^2)}} \tag{3.19}$$

For a nonrelativistic charged particle, the equation 3.17 can be written approximately as:

$$\frac{dE}{dx} = \frac{-Z^2AD}{E^{\alpha-1}} \tag{3.20}$$

Here α and D are constants for a given material, Z is the particle charge and A is the particle mass number. Rearranging and integrating equation 3.20, the following equation can be obtained:

$$Z^2A = \frac{(E+\Delta E)^\alpha - E^\alpha}{D\alpha\Delta x}. \tag{3.21}$$

In the case of a charged particle absorbed in a ΔE-E telescope, Δx was understood as the charged particle path length in the ΔE scintillator. ΔE is the energy deposited in the ΔE scintillator. E is total energy stopped in the E scintillator. PID is defined as Z^2A, which was used to identify a particle. For example, a PID value near 1 indicates that the particle is likely a proton.

The PID value for the particle hitting SALAD ΔE-E telescope in experiment 003 can be histogramed. This process was used to identify a proton from the photodisintegration of a Deuteron. After the ΔT_{good} cut in Figure 3.8 and a random coincidence subtraction have been performed, the PID histogram for the particles hitting the SALAD ΔE-E telescope can be obtained, and it is shown in Figure 3.9(a).

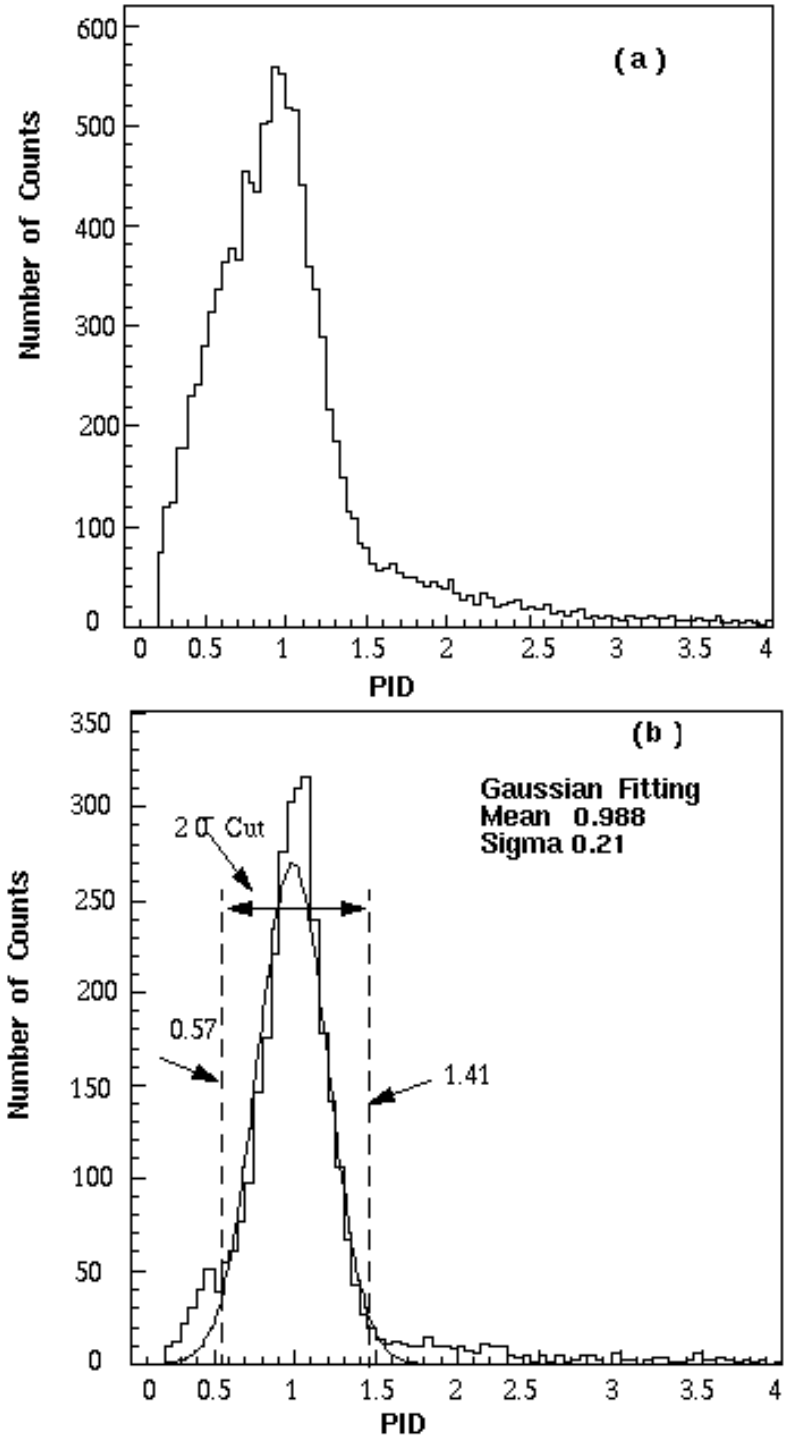

Figure 3.9: PID histograms a) before and (b) after the cut on the difference between calculated and measured proton energy

Another cut was added to eliminate the electron and other charged particle background in Figure 3.9(a). This cut required the difference between the calculated and measured proton energy to be between -5.51 MeV and 3.81 MeV. This cut will be explained in more detail later. The PID histogram after the energy difference cut is shown in Figure 3.9(b).

A Gaussian fit is performed on the histogram in Figure 3.9(b). The standard deviation of this Gaussian distribution is σ. The area between $\pm 2\sigma$ Gaussian distribution is 95.5%. The PID cut for a proton detected in SALAD is set between $\pm 2\sigma$, which is a PID value between 0.57 and 1.41. Two criteria are considered for this proton PID cut. One is that there should be enough proton events left to obtain enough related neutrons impinging on the neutron detector. Another is that the particles identified as protons should not be contaminated by electrons and other charged particle backgrounds.

The following cut on the difference between calculated and measured proton energy was added to eliminate the remaining electron and other charged particle background contamination. If an event was due to the photodisintegration of a Deuteron, the outgoing proton energy can be calculated from the photon energy as determined from the tagger, and the outgoing proton angle as determined from the SALAD wire chambers, by using the two body kinematics. This energy should be the same as the energy measured from the SALAD ΔE-E telescope. A histogram of the difference between the proton energy calculated from two body kinematics and the energy measured from the SALAD ΔE-E telescope is shown in Figure 3.10(a). This histogram is made with the following conditions: $474 <$ tagger TDC < 676 and $0.57 <$ PID < 1.41. If a random background, i.e. $798 <$ tagger TDC < 1000, was subtracted from Figure 3.10(a), another histogram for the difference between calculated and measured proton energy can be obtained, which is shown in Figure 3.10(b). A Gaussian fit is performed on the histogram in Figure 3.10(b). The standard deviation of this Gaussian fit is σ, the difference between calculated and measured proton energy in SALAD is set between $\pm 2\sigma$, which is between -5.51 MeV and 3.81 MeV.

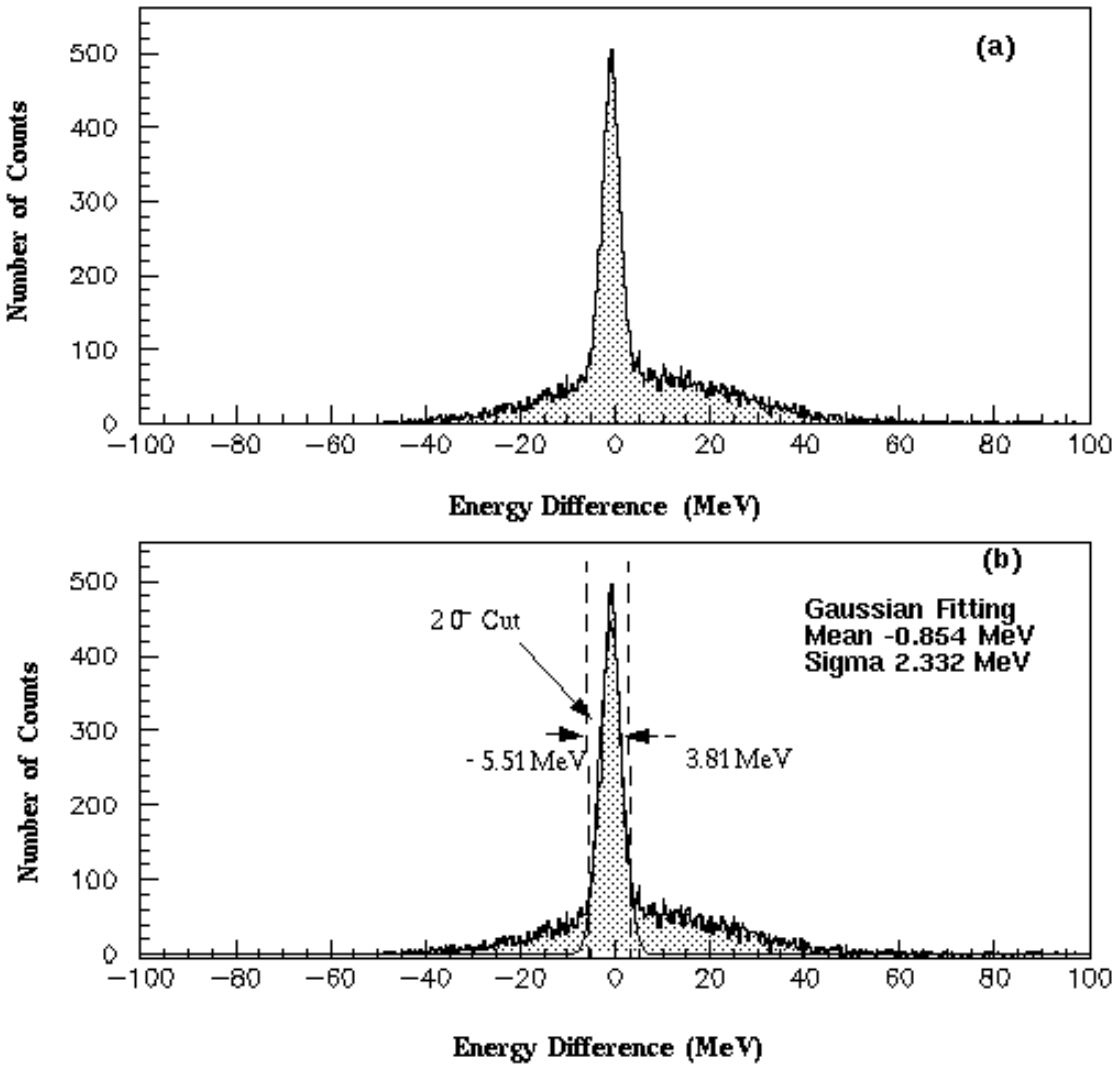

Figure 3.10: Histogram showing the difference between calculated and measured proton energy (a) before and (b) after random subtraction was performed.

3.4.2 The Number of Neutrons Impinging on the Neutron Detector

When a proton from the photodisintegration of a Deuteron was identified by SALAD, the related neutron energy and direction could be calculated from the photon tagger energy and the outgoing proton angle by using two body kinematics. The outgoing neutron was checked to see if it hit the neutron detector or not. The energy distribution of incident neutrons which did hit the SAL neutron detector is shown in Figure 3.11 after the random background subtraction in Figure 3.8. The neutron number impinging on the neutron detector can be obtained from Figure 3.8 as a function of the incident neutron energy. Only a small percentage of these incident neutrons interacted with the SAL neutron detector and deposited enough energy to be detected.

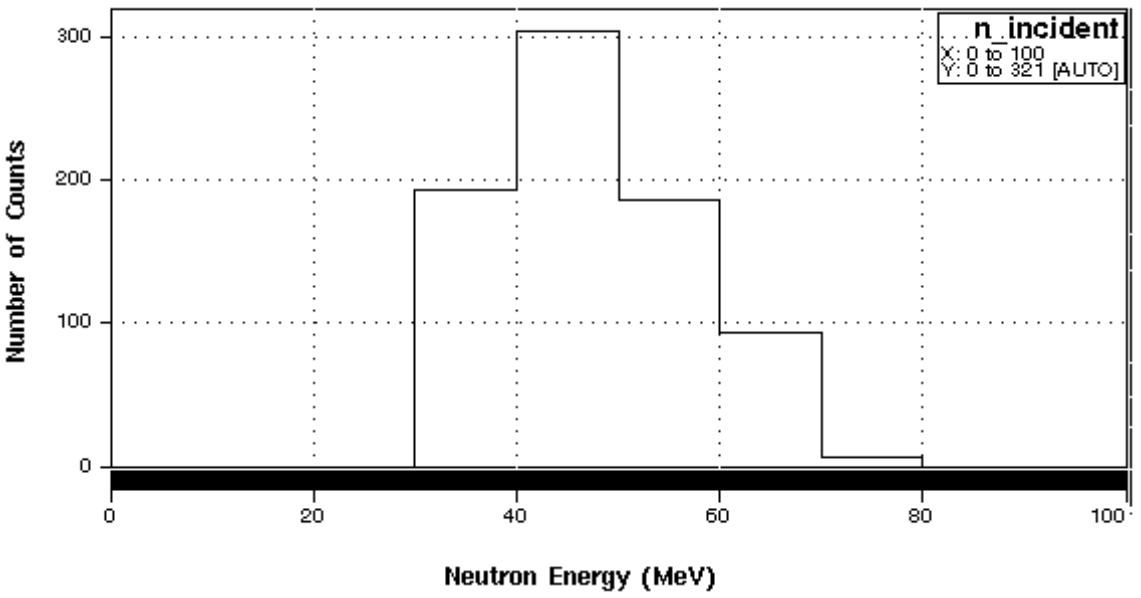

Figure 3.11: The energy distribution of the neutrons impinging on the neutron detector.

3.4.3 The Number of Neutrons Detected by the Neutron Detector

The following conditions identify a neutron detected by the SAL neutron detector.

1. If a proton was identified by SALAD and the related neutron was found impinging on the SAL neutron detector, the neutron detector TDC would be checked to see if the neutron was detected or not. If the neutron was seen in the neutron detector TDC, its energy could be calculated from the neutron time of flight from the target to the detector. The outgoing neutron energy can also be calculated from the photon tagger energy and the outgoing proton angle. The difference between the neutron energy calculated from two body kinematics and the neutron energy calculated from time-of-flight is shown in Figure 3.12. If the magnitude of this energy difference was less than 40 MeV, which accounted for finite time-of-flight resolution and position resolution, the neutron was considered to be detected. This energy difference cut was made in the same way as in the simulation.

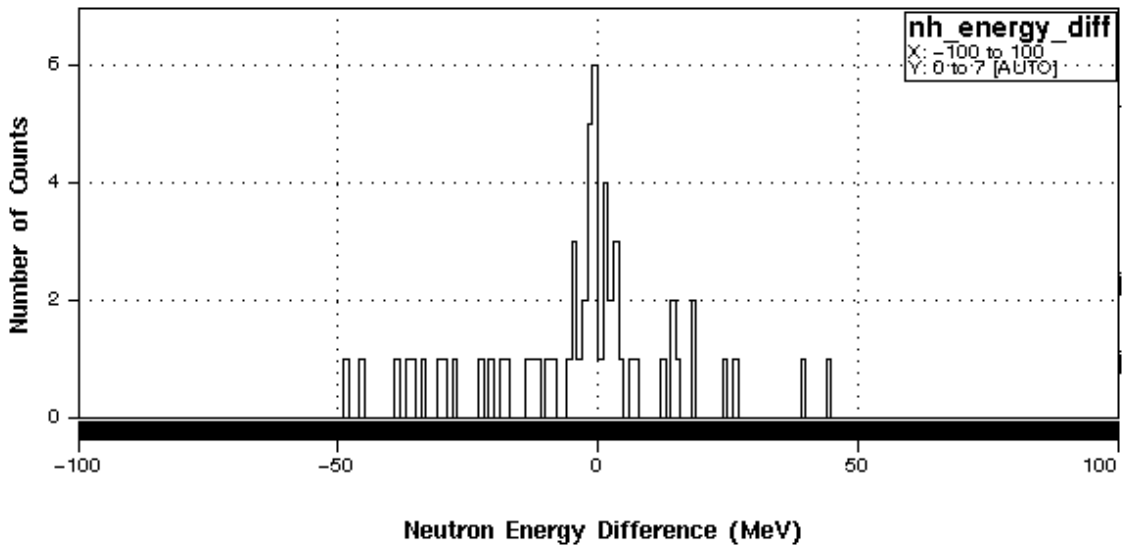

Figure 3.12: The difference between the neutron energy calculated from two body kinematics and the neutron energy calculated from time-of-flight.

2. If the particle detected in the neutron detector E bars was in fact a neutron, there should not be an ADC response in the veto detector at the same bar position where the neutron was detected.

If a neutron was detected in the SAL neutron detector, its energy distribution could be found. The detected neutron energy distribution is shown in Figure 3.13 after the random background subtraction in Figure 3.8. The neutron number detected by the neutron detector can be obtained from Figure 3.13 as a function of the incident neutron energy.

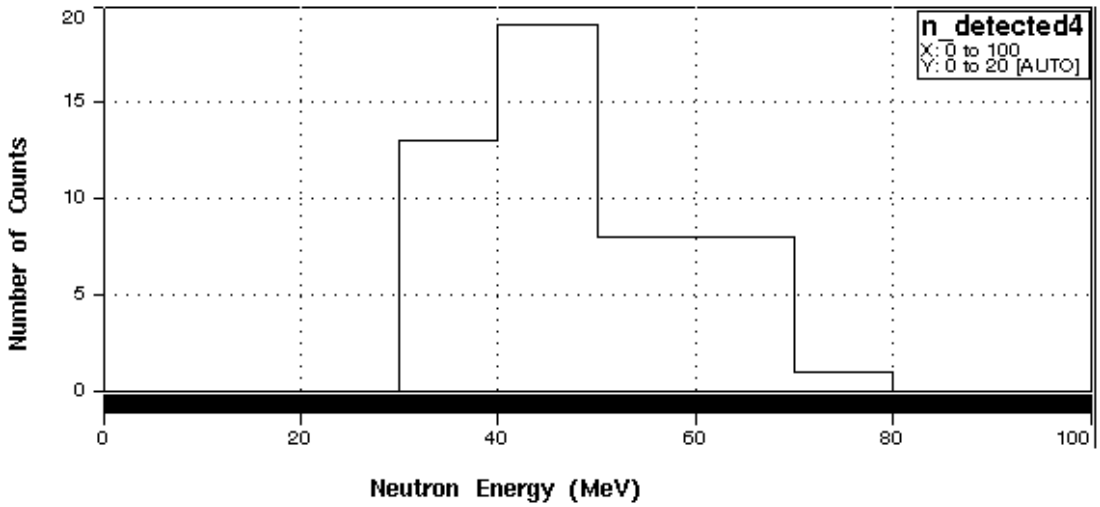

Figure 3.13: The energy distribution of the neutrons which were detected in the SAL neutron detector.

3.4.4 The SAL Neutron Detector Efficiency

The SAL neutron detector efficiency can be obtained from Figure 3.11 and Figure 3.13 and will be compared to the simulation results in Chapter 5.

Chapter 4

Experiment 003 Computer Simulation

4.1 Introduction

In this chapter, I will discuss the simulation of the response of the SAL neutron detector in the configuration used in experiment 003. The neutron detector efficiency will be calculated and compared to the results of experiment 003. The simulation program was run on the SUN Microsystems UNIX workstation at the Saskatchewan Accelerator Laboratory. This simulation program used the PATCHY code management system, the GEANT subroutine library and FORTRAN 77. Simulation histograms were displayed by using PAW. The GEANT and PAW software packages were developed at CERN. A detailed description of PAW is given in Reference [11]. A detailed description of the GEANT subroutine library is given in Reference [5] and Reference [2].

4.2 Simulation Setup

The coordinate system used in the simulation is the same as the system used for experiment 003 which was shown in Figure 2.1. The length unit in the GEANT simulation is cm and the particle energy and mass units are GeV and GeV/c^2. The program is divided into the following eight parts: common blocks, GEANT initialization, detector setup, event generation, hit data structure, detector response, tracking and data output.

Common Blocks : The data communication between GEANT subroutines is by common blocks. GEANT defines about 40 common blocks by itself. Ordinary GEANT common blocks and subroutines begin with 'G'. Additional common

blocks defined by the user communicated between subroutines for extra computation tasks.

Initialization : A series of GEANT initialization subroutines were used to initialize the GEANT default common blocks, read format, dynamic core divisions, drawing packages, standard particle and ion data, and the cross section tables. The default input data can be defined in the user subroutine NEWCAR. An additional data input file was named 'salad.dat'. In 'salad.dat', 22 input data items were used for general control purposes in GEANT; these are: the general control of the run, the control of physics processes, debugging and I/O operations. These 22 input data items did not need to use the GEANT function FFKEY to transfer data items into GEANT. Another 16 input data items were used for experiment 003 definitions which included the target type, the incident particle energy distribution selections, the incident particle type and the outgoing particle types etc. These 16 input data items used the GEANT function FFKEY to transfer data items into GEANT.

Detector Setup : The detectors' geometry, material, and relative positions were set after the GEANT initialization subroutines. The details are presented below

1. The geometry of SALAD and the geometry of the SAL neutron detector were set. The GEANT standard shapes are a box, a trapezoid, a tube or a cylinder. The geometry information is stored in common blocks. Examples of these geometries are given in Figure 4.1 and Figure 4.2. Fig 4.1 is the three dimensional geometry of the SALAD E scintillator. Fig 4.2 is the three dimensional geometry of the SAL neutron detector. These pictures were obtained by using the GEANT subroutine GDSPEC.

2. The materials making up SALAD and the SAL neutron detector were set. There are only 16 predefined materials in GEANT. The other materials in SALAD and the SAL neutron detector that did not show up in the GEANT standard list were defined separately. The materials that needed

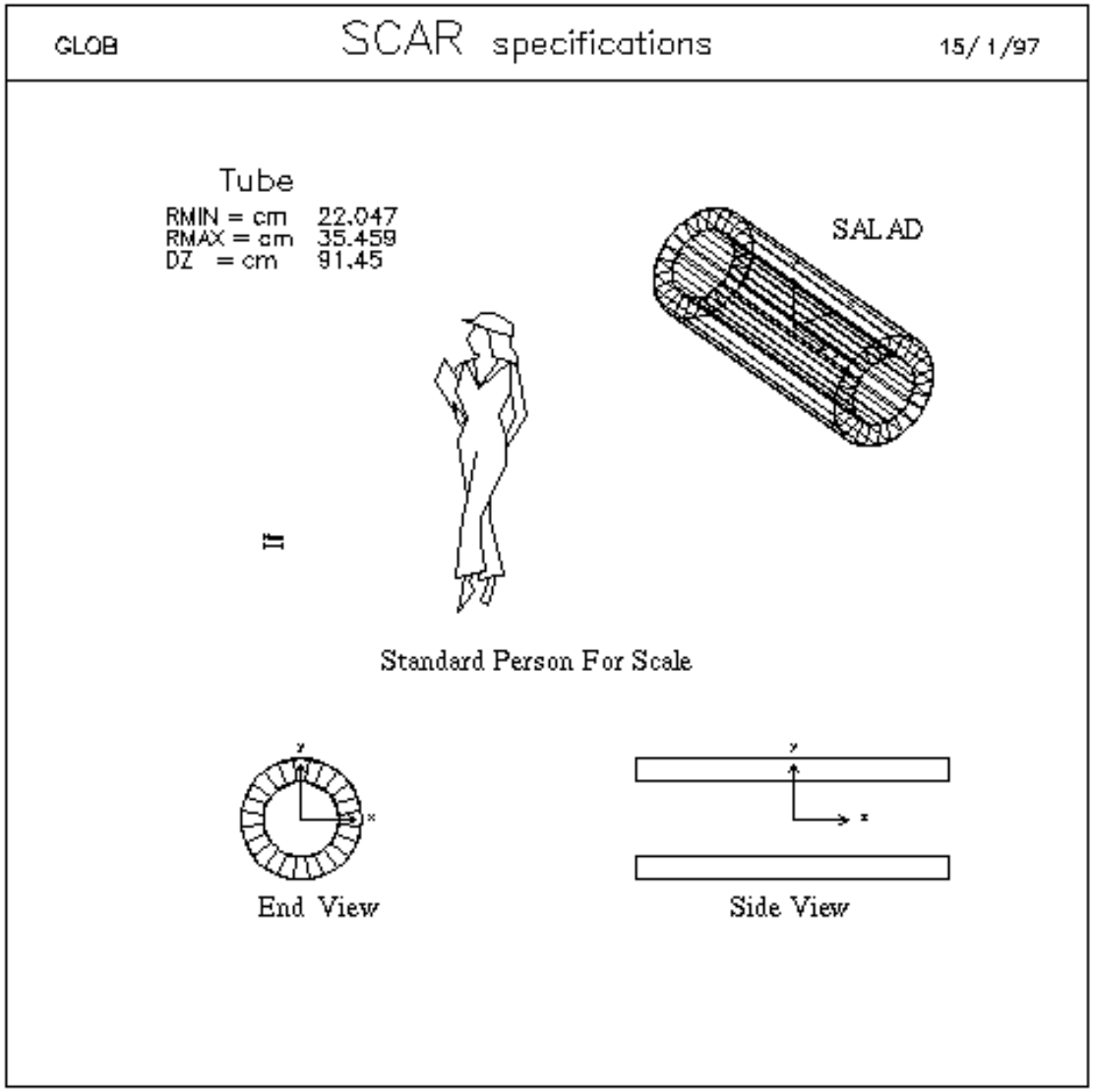

Figure 4.1: SALAD E scintillator geometry in GEANT.

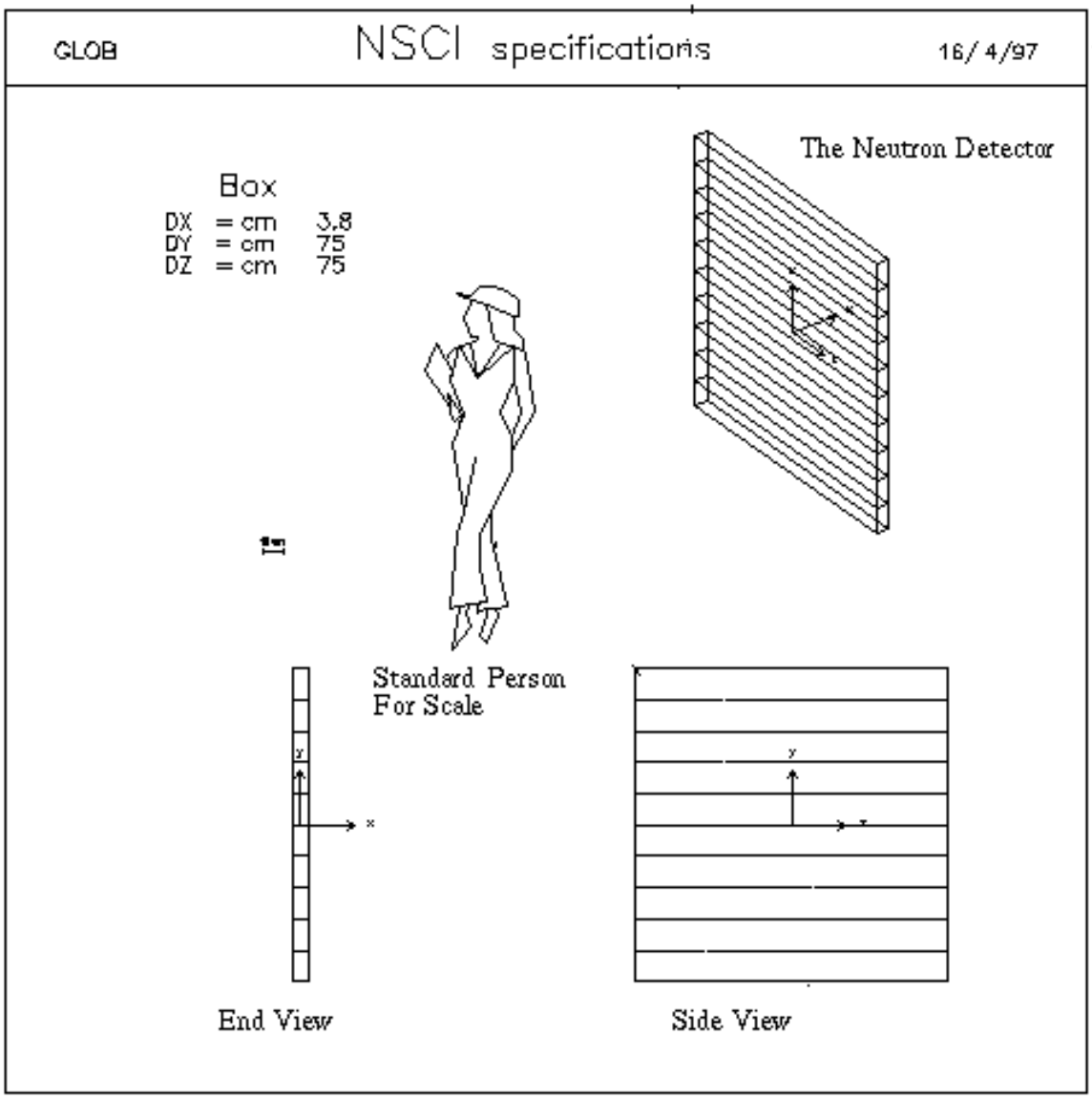

Figure 4.2: The SAL neutron detector geometry in GEANT.

to be defined in this simulation were: PVC Plastic, Mylar, Polystyrene, Kapton, the Deuterium target gas at an absolute pressure of 7 atm and at a temperature of 25^0 C, Isobutane-Argon gas mixtures in the wire chambers and BC-408 and BC-412 Scintillators. The GEANT subroutine GSMIXT served this purpose. For each material, the density and the relative number of each component element were defined. The GEANT subroutine GSTMED assigned each new material a 4-character name and a tracking medium number. This tracking medium number would be used when the GEANT subroutine GSVOLU defined a volume shape and filled the volume with this material. The GEANT subroutine GSPOS was used to put the volume into its mother volume so that their related positions could be set. Because of the symmetry of the SAL neutron detector geometry, the GEANT subroutine GSDVN was used to divide the neutron detector into ten bars.

Event Generation : GEANT automatically called the subroutine GUKINE which had to be written by the user for generating an event. Inside the subroutine GUKINE, the GEANT subroutine GSVERT was called to store a vertex position (x, y, z), i.e. where the $^2H(\gamma, pn)$ reaction took place. The photon beam in experiment 003 was assumed to be spread in a Gaussian distribution in the x and y directions and to be uniform in the longitudinal direction. Events were generated by the GEANT subroutine GENBOD. This subroutine generated a N-body event according to a Fermi-Lorentz invariant phase space. Events were generated in their own center-of-mass system and were transformed to the lab system. The outgoing particles' momentum and energy were stored. In this simulation, the outgoing particles which were generated by GENBOD were a neutron and a proton.

Hit Data Structure : The GEANT subroutines GSDET and GSDETH were used to define the hit pattern within a detector. These two subroutines were used

mainly for building the data structure. GSDET built the data structure JSET for each detector. GSDETH was used to define the hit variables such as the position and energy in each hit. In this simulation, GSDETH was used to set up 9 variables, which were: hit position x (cm), hit position y (cm), hit position z (cm), energy deposited (GeV), kinetic energy (GeV), track volume flag, step size (cm), time to transverse step (ns), and particle types. The GEANT subroutine GSAHIT was used to store these variables for each hit.

Tracking : GEANT automatically called the subroutine GUTREV which had to be written by the user to control event tracking. In GUTREV, the user subroutine HEINIT was used to initialize the variables before each track. The GEANT subroutines GTREVE and GTRACK were called to track particles. At the end of each tracking, GEANT automatically called the subroutine GUSTEP which had to be written by the user. In the subroutine GUSTEP, the GEANT subroutine GSXYZ was used to transfer tracking data from the common block to the data structure JXYZ so that the data could be used to debug or draw trajectories. The GEANT subroutine GDCXYZ was called to draw tracks. The user subroutine DHITS in GUSTEP was used to calculate the quantities such as the energy deposited in the detector or the path length in the detector at each step rather than at the end of an event.

Detector response : GEANT automatically called the subroutine GUOUT which had to be written by the user to control the response of a detector before the end of an event. In the user subroutine GUOUT, the GEANT subroutine GFHITS was called to fetch the values stored in the JHITS data structure, which were the 9 variables stored by the GEANT subroutine GSAHIT in this simulation. The total energy loss in the detector and the ADC reading from the both ends of the detector can be calculated from these values. The responses of the SALAD wire chambers, the SALAD E scintillators, the SALAD ΔE scintillators, the SAL neutron detector bars and the veto detectors were simulated in the subroutine

GUOUT.

Data output : The GEANT subroutine HBOOK1 was used to declare a one dimensional histogram. The GEANT subroutine HFILL was used to fill the existing histogram. The histograms were stored in the file named as 'for009' which could be displayed by PAW. The user subroutine UGLAST was used to terminate a run. The standard GEANT termination subroutine GLAST was called in the subroutine UGLAST. The SAL neutron detector efficiency can be calculated in UGLAST.

4.3 Simulation Results

The energy range of the incident photons determines the energy range of neutrons which will be incident on the neutron detector in the simulation. The incident photon energy distribution was made the same as the photon energy distribution in experiment 003. This allowed a direct comparison of the simulation results to the experiment results. The incident photon energy distributions in the simulation and the experiment are shown in Figure 4.3.

A sample simulation diagram showing particle tracks for experiment 003 is shown in Figure 4.4. In Figure 4.4, a solid line represents a proton, a long dashed line represents a neutron and a short dashed line represents a γ ray. Most protons are stopped by the SALAD E scintillators and the SALAD iron cylindrical shield, so the number of protons passing out of SALAD is far less than the number of neutrons passing out of SALAD, which can be seen in Figure 4.4.

4.3.1 Simulation Results for SALAD

The energy deposited by a proton in the SALAD ΔE scintillator in this simulation is shown in Figure 4.5 compared to the results from experiment 003. The energy deposited by a proton in the SALAD ΔE scintillator in experiment 003 can be obtained

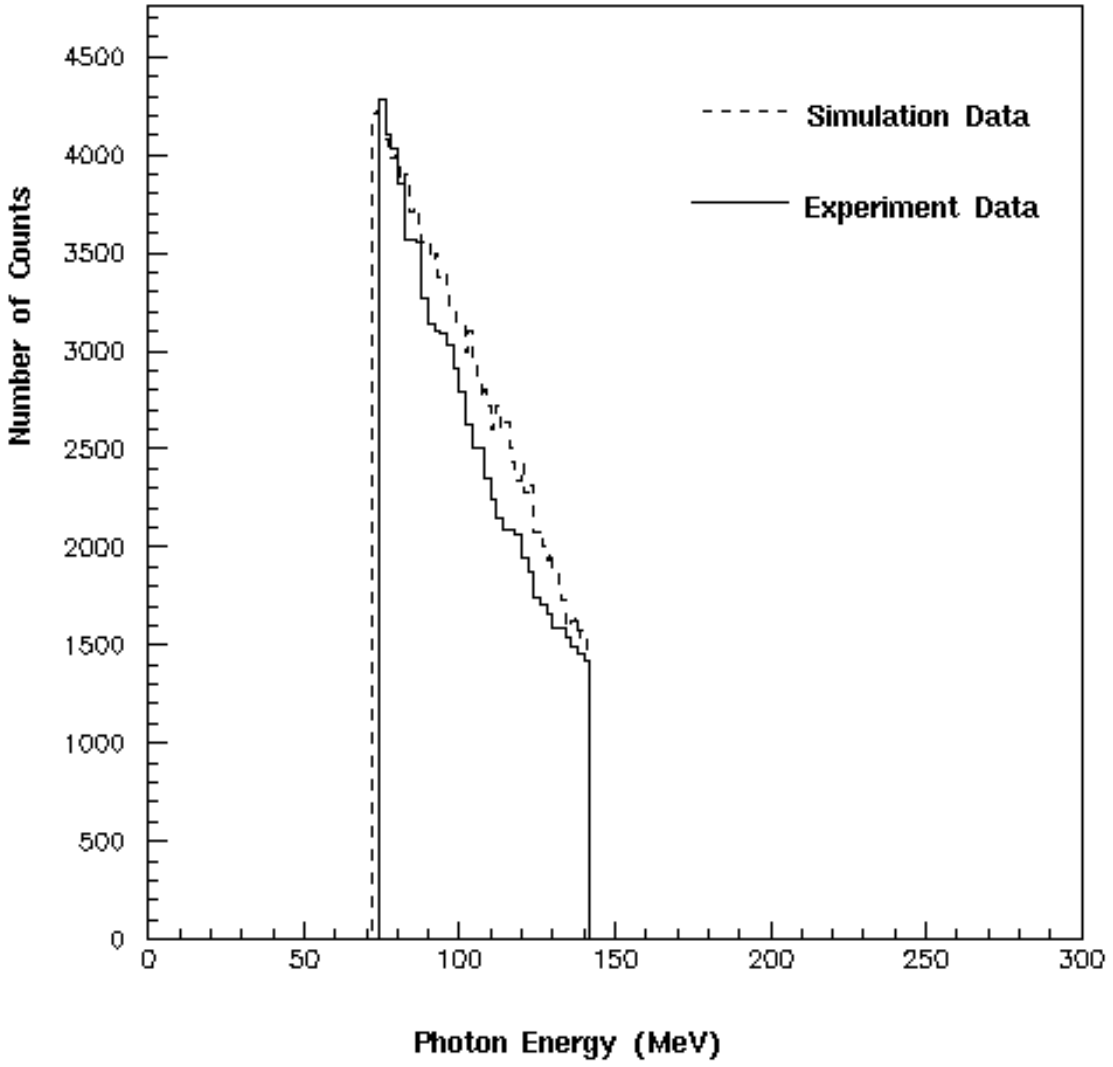

Figure 4.3: The incident photon energy distribution in the simulation compared to that in experiment 003.

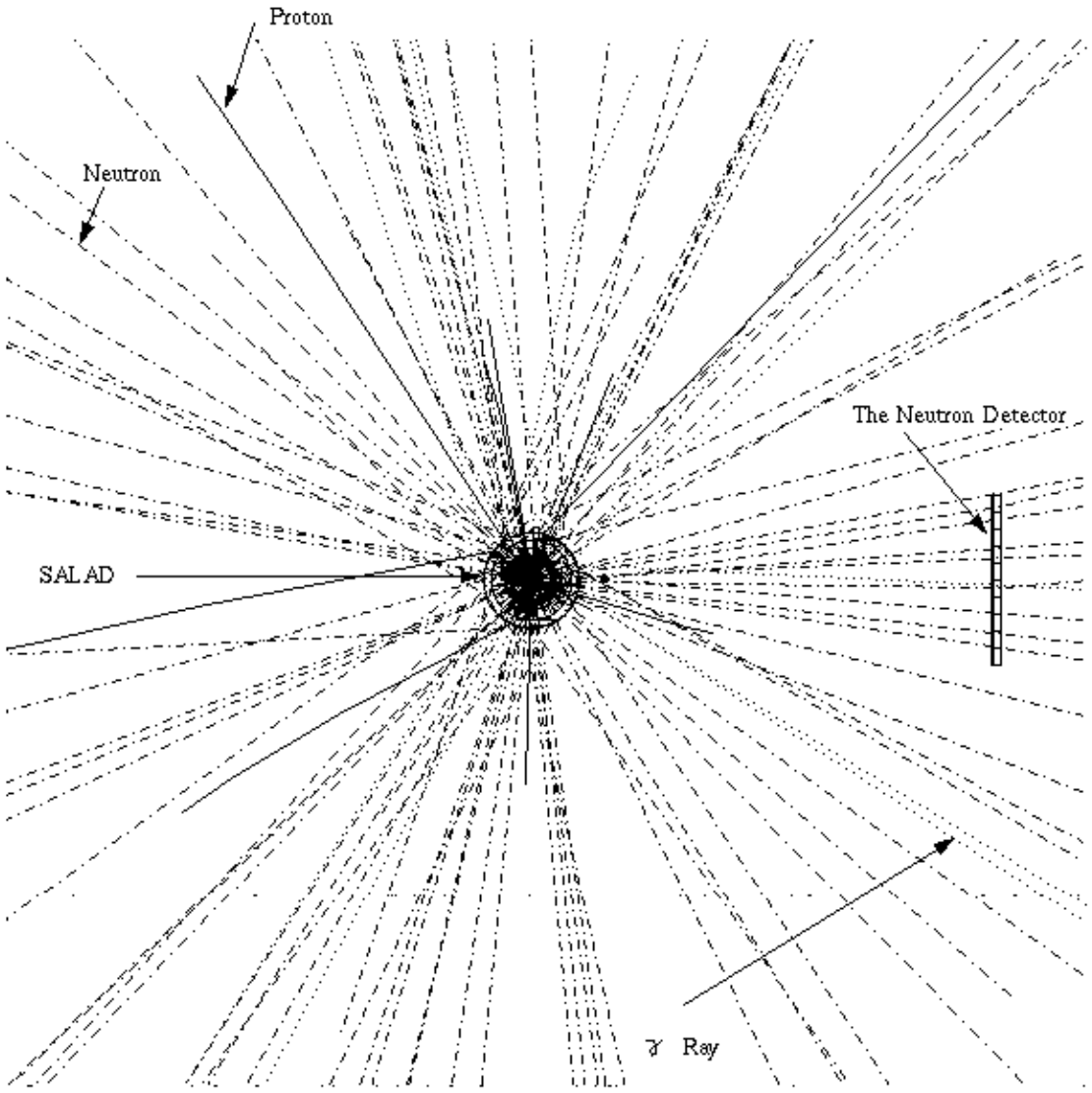

Figure 4.4: Experiment 003 tracking simulation diagram: a solid line represents a proton, a long dashed line represents a neutron and a short dashed line represents a γ ray.

from the ΔE scintillator ADC output and the ΔE scintillator gain calibration from Equation 3.12.

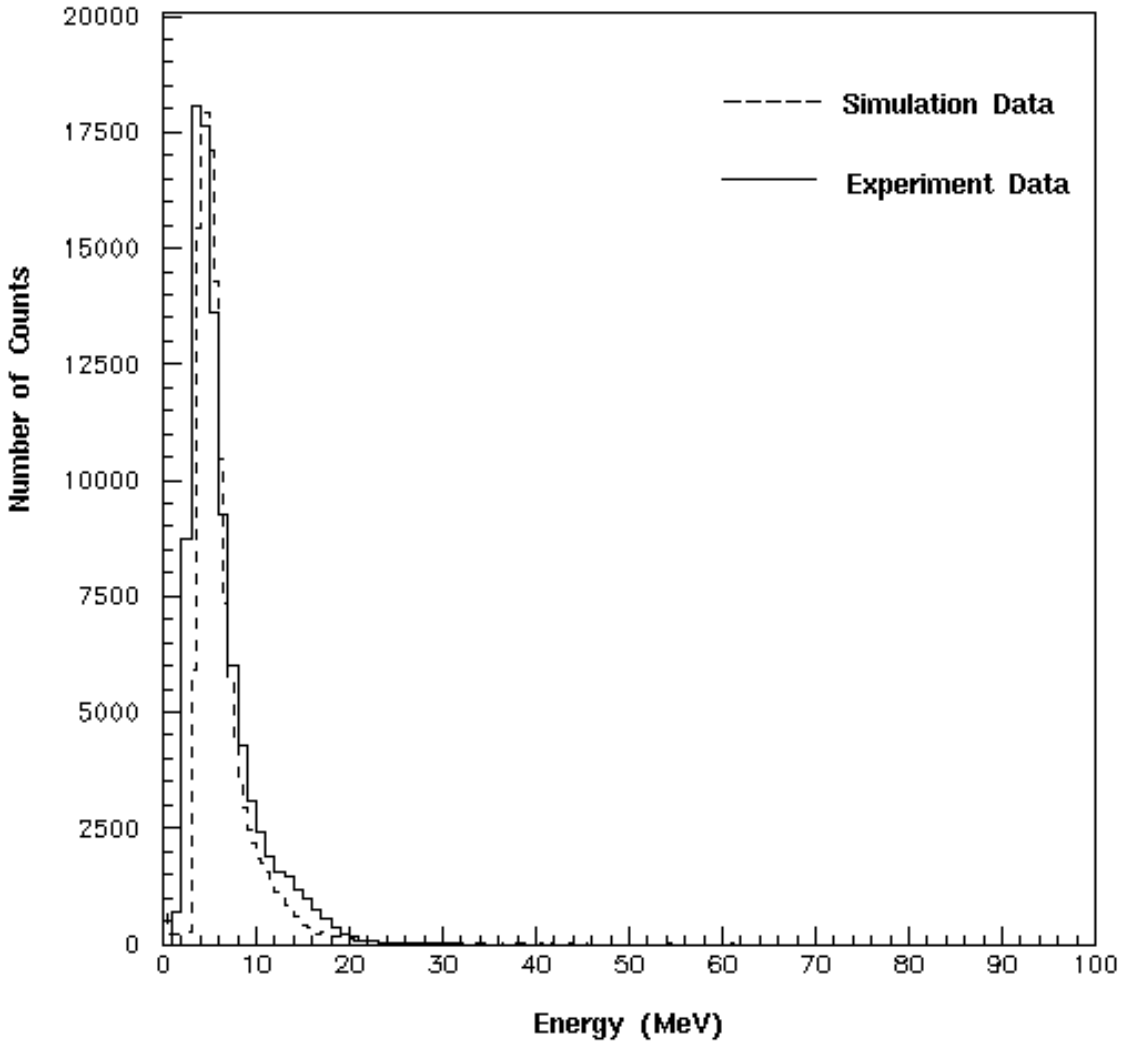

Figure 4.5: The energy deposited by a proton in the SALAD ΔE scintillator from the simulation compared to that from experiment 003.

A similar comparison for the energy deposited by a proton in the SALAD E scintillator is shown in Figure 4.6.

The light output in equivalent electron energy (MeV_{ee}) in the plastic scintillator detector per unit length is related to the energy deposited in the detector and the

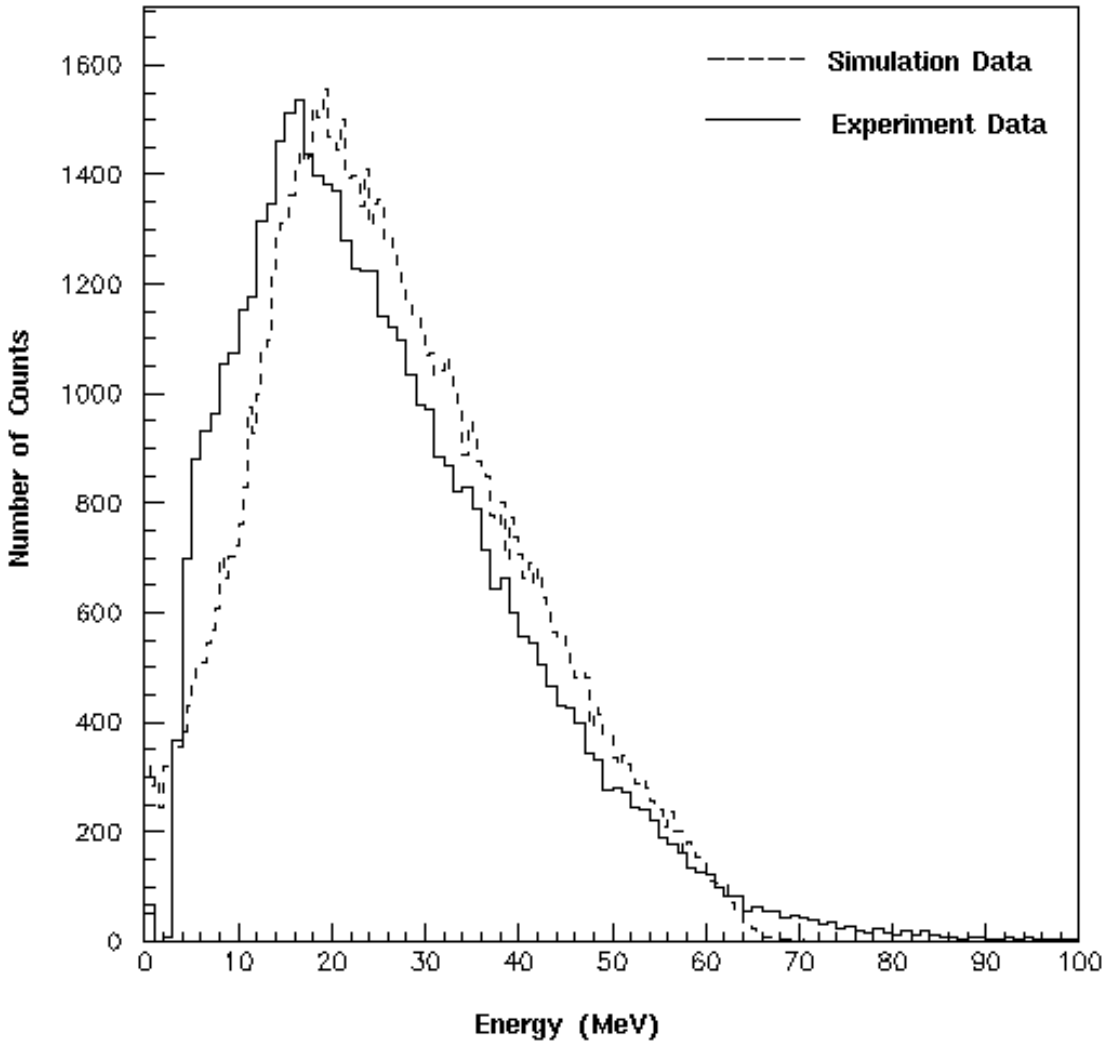

Figure 4.6: The energy deposited by a proton in the SALAD ΔE scintillator from the simulation compared to that from experiment 003.

ionization type. The relation used in this simulation is shown below.

$$\frac{dL}{dx} = \frac{S\frac{dE}{dx}}{1 + B\frac{dE}{dx} + C\frac{dE}{dx}^2} \tag{4.1}$$

Here $\frac{dE}{dx}$ is the stopping power, i.e. the energy deposited per unit length divided by the detector density, and is in units of $MeV\ cm^2/g$. $\frac{dL}{dx}$ is the light output in equivalent electron energy per unit length divided by density and is in units of $MeV_{ee}\ cm^2/g$. S, B and C are constants. S is equal to 1.0346, B is equal to 1.09E-2 and C is equal to 7.95E-6 for a proton hit in the SALAD E scintillator. A more detailed explanation for the response of a plastic scintillator to protons and deuterons can be found in the paper by G.V. O'Rielly, N.R. Kolb and R.E. Pywell [6].

The simulation results for the total light output for a proton in the SALAD ΔE scintillator and E scintillator are shown in Figure 4.7.

The light attenuation lengths for Bicron-408 and Bicron-412 plastic scintillators are 380 cm and 400 cm respectively. The SALAD upstream and downstream ADC output can be obtained from equation 3.9 and equation 3.10 by using the attenuation length, the scintillator gain calibration and the total light output. An example of simulation results for the ADC outputs in SALAD upstream ΔE scintillators and upstream E scintillators is shown in Figure 4.8 in comparison to the results from experiment 003.

4.3.2 Simulation Results for the SAL Neutron Detector

If a neutron in this simulation is found to be heading towards the neutron detector from the reaction kinematics, its angular and position distributions in the neutron detector can be found, and these are shown in Figure 4.9. The energy distribution of these neutrons is shown in Figure 4.11(a).

Only a small percentage of incident neutrons interacted with the neutron detector. The GEANT simulation of a neutron interaction with a detector uses the following code: INEG (inelastic processing), ELAG (elastic processing), FISG (fission process-

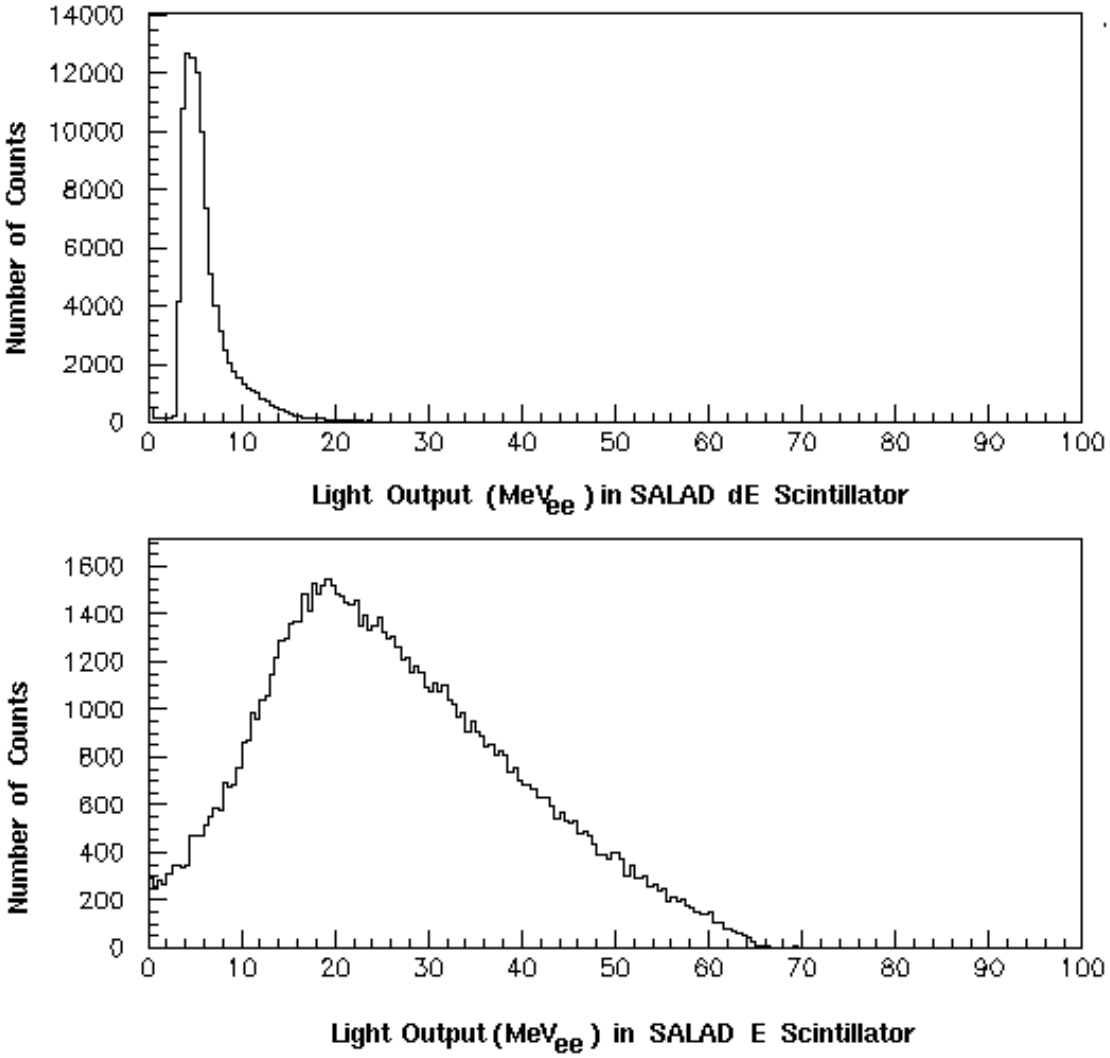

Figure 4.7: The simulation results for the total light output for a proton in the SALAD ΔE scintillator and E scintillator.

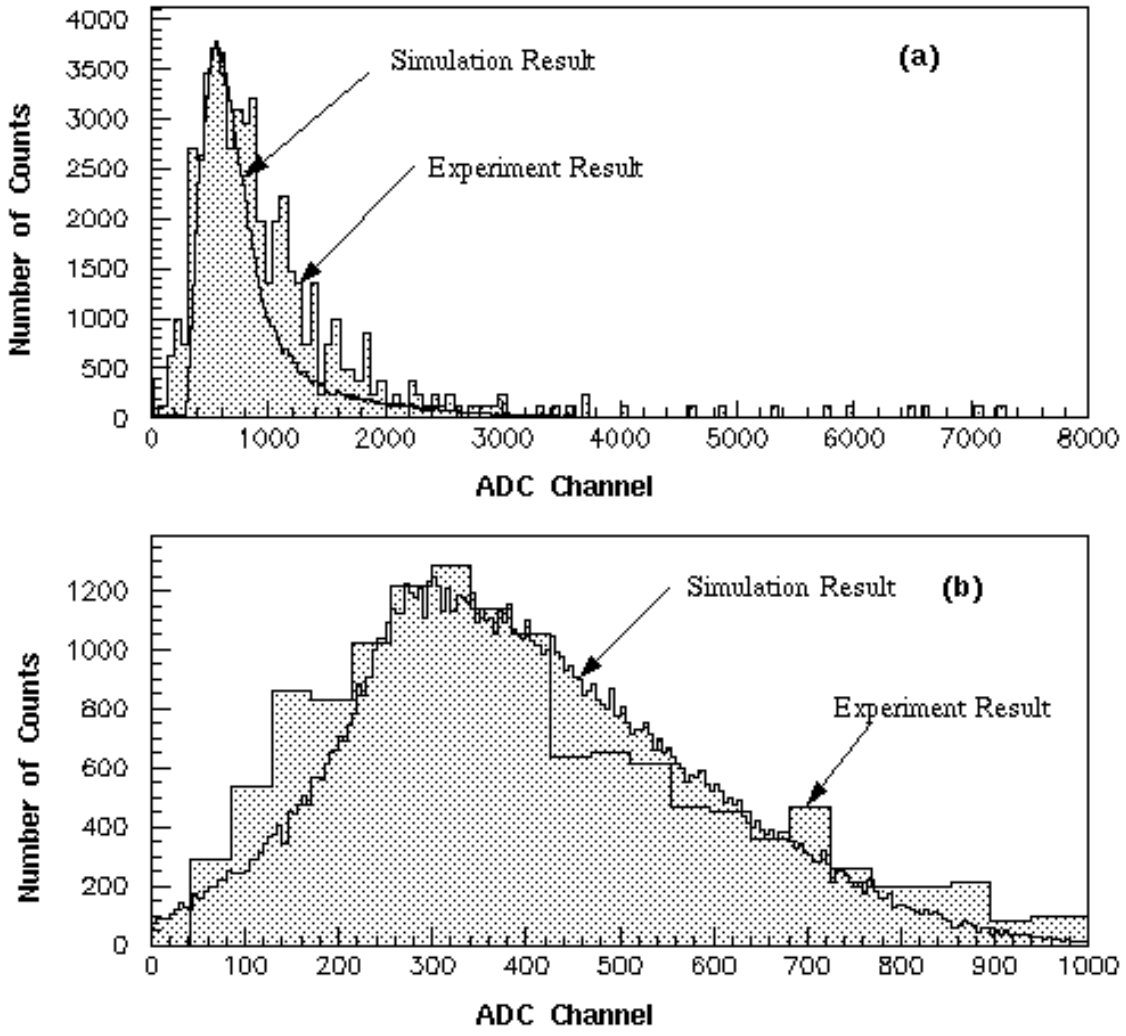

Figure 4.8: An example of simulation results for the ADC outputs in SALAD (a) upstream ΔE scintillators and (b) upstream E scintillators.

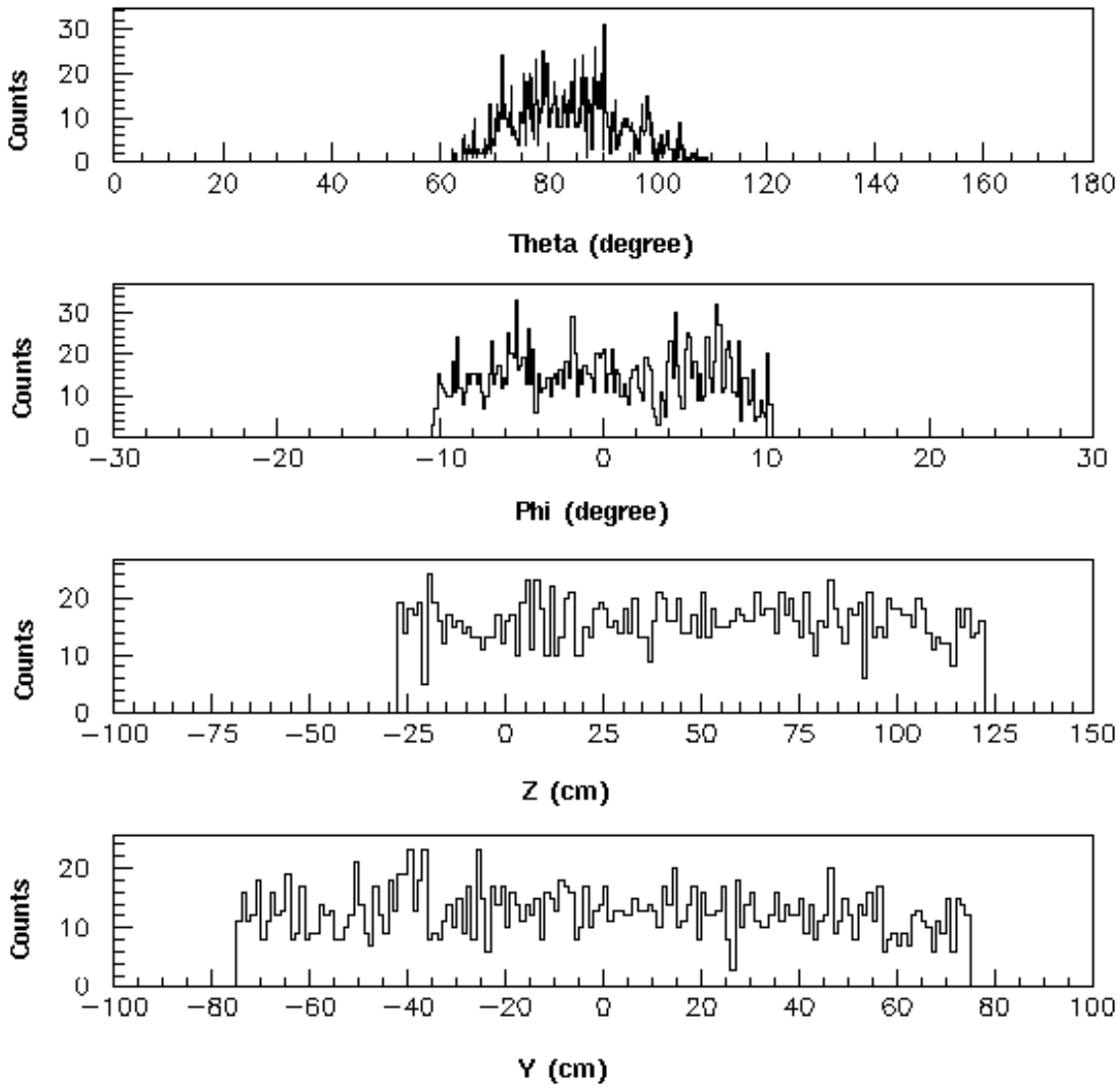

Figure 4.9: Incident neutron angular and position distributions in the SAL neutron detector.

ing), CAPG (capture processing) and HADG (all processing). Interaction neutrons deposited only part of their energy in the neutron detector bars. The ratio between the neutron energy deposited in the neutron detector bars and the incident neutron energy is shown in Figure 4.10.

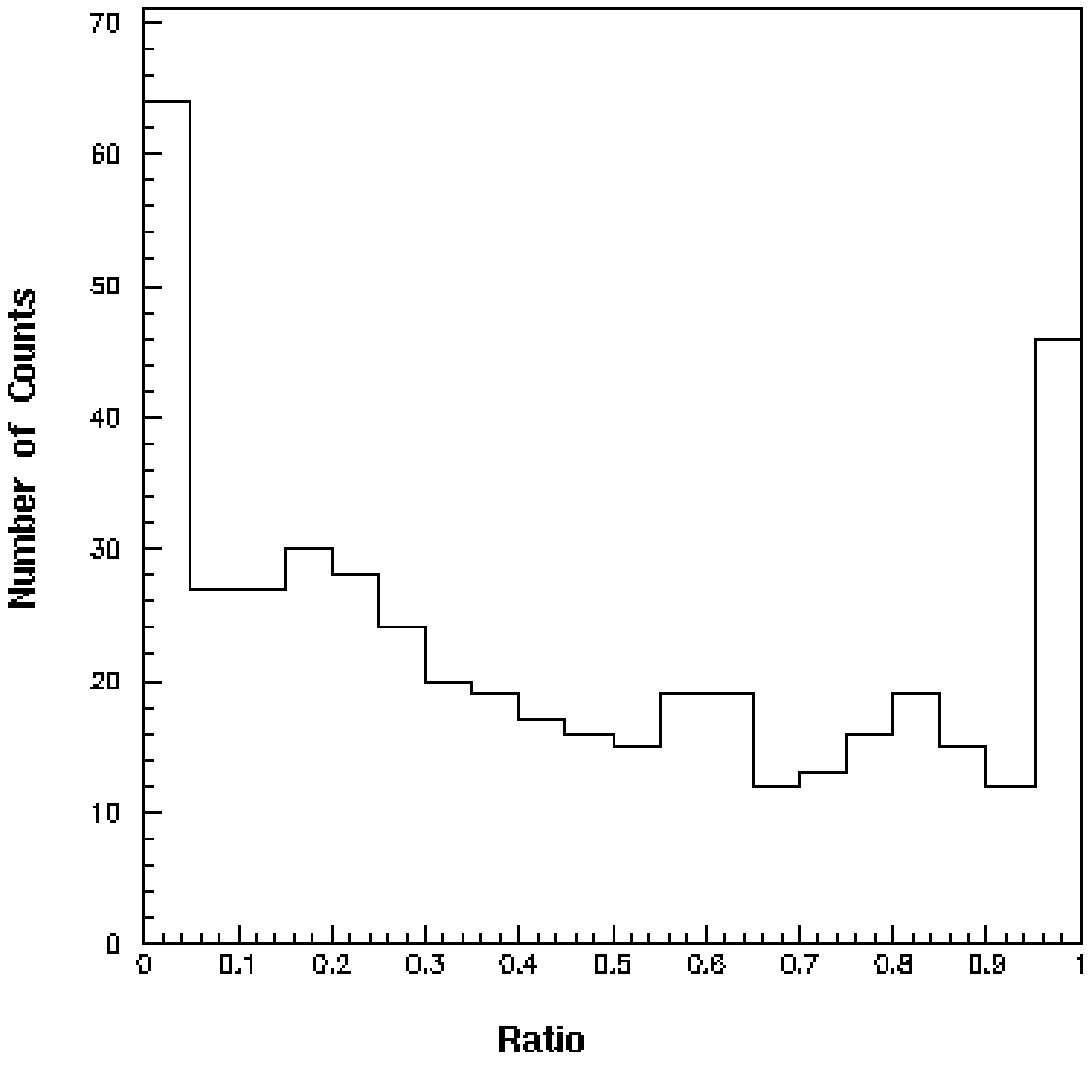

Figure 4.10: The ratio between the neutron energy deposited in the neutron detector and the incident neutron energy.

If a neutron deposited energy more than 2 MeV in the neutron detector, it would cause a SAL neutron detector TDC response and its energy distribution could be recorded. The energy distribution of the neutrons which were detected in the neutron

detector is shown in Figure 4.11(b). The threshold energy 2 MeV was the same as that used in experiment 003.

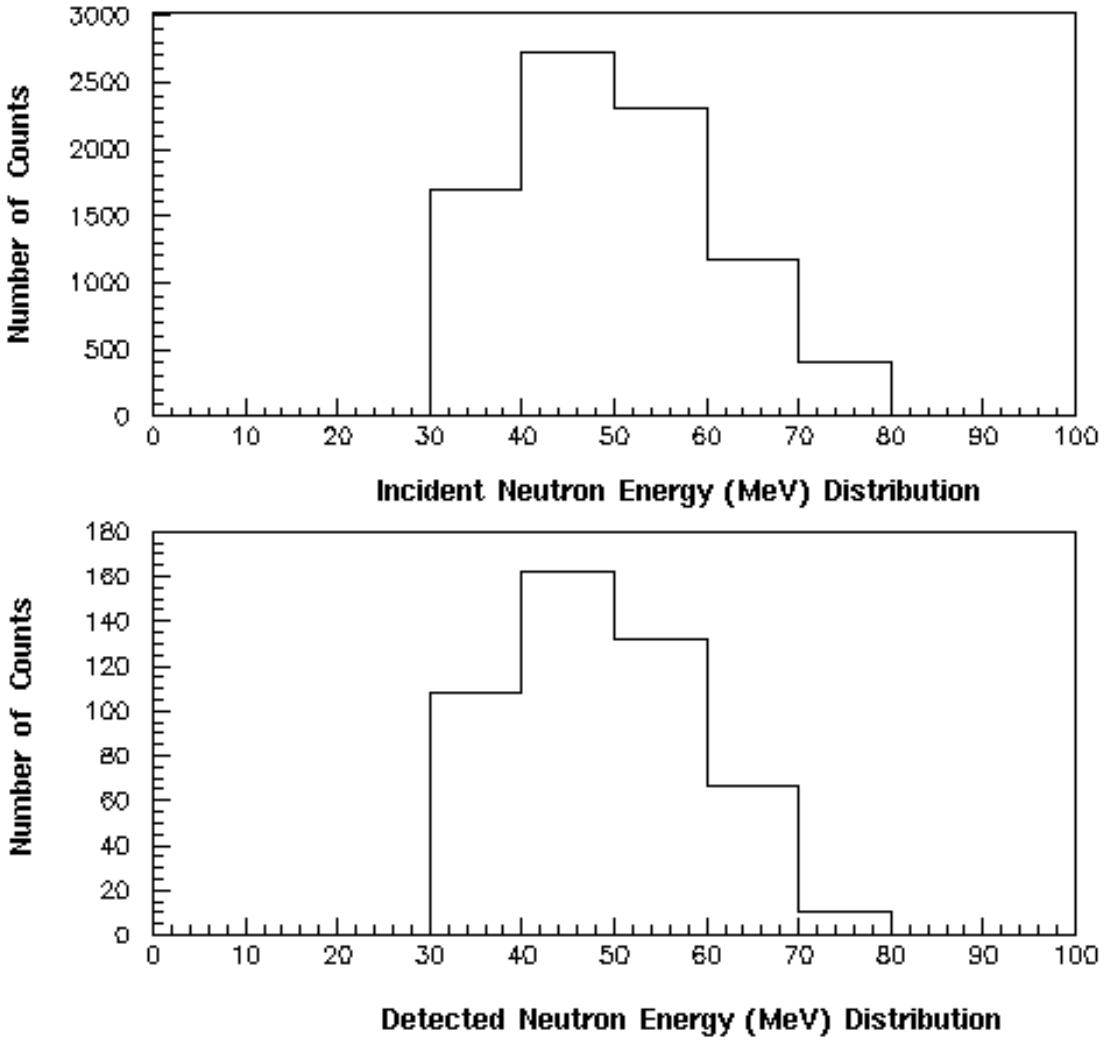

Figure 4.11: Incident and detected neutron energy (MeV) distributions in the SAL neutron detector.

The SAL neutron detector efficiency can be calculated from Figure 4.11(a) and Figure 4.11(b) in this simulation. The result will be compared to the result of experiment 003 and will be discussed in Chapter 5.

Chapter 5

Neutron Detector Efficiency Results

5.1 The Neutron Detector Efficiency

The neutron detector intrinsic efficiency, ϵ, can be calculated from equation 1.4 in Chapter 1. That is:

$$\epsilon = \frac{neutrons\ counted}{neutrons\ on\ the\ detector} \tag{5.1}$$

Here *neutrons counted* is the number of neutrons detected by the neutron detector, and *neutrons on the detector* is the number of neutrons actually impinging on the neutron detector.

In experiment 003, the outgoing neutron direction was calculated from the tagged photon energy and the outgoing proton angle by using two body kinematics. The outgoing neutron was checked to see if it hit the neutron detector or not. The number of neutrons hitting the neutron detector that was calculated from the vertex, i.e. from two body kinematics, was greater than the number of neutrons actually hitting the neutron detector. This is because the outgoing neutrons may interact with the SALAD detector materials or iron cylindrical shield and may be deflected from their original direction and then may not hit the neutron detector. Another neutron detector efficiency ϵ_1 had to be defined to meet the experiment condition.

$$\epsilon_1 = \frac{neutrons\ counted}{neutrons\ on\ the\ detector\ from\ vertex} \tag{5.2}$$

Here *neutrons on the detector from vertex* is the number of neutrons heading towards the neutron detector calculated from the reaction kinematics.

The neutron detector efficiency, ϵ_1, as a function of the incident neutron energy,

can be obtained from experiment 003 by comparing the number of neutrons detected in the neutron detector shown in Figure 3.13, and the number of neutrons heading towards the neutron detector from the reaction vertex shown in Figure 3.11. The neutron detector efficiency, ϵ_1, can also be obtained from the simulation by comparing the number of neutrons detected in the neutron detector shown in Figure 4.11 (b) and the number of neutrons heading towards the neutron detector shown in Figure 4.11 (a).

The neutron detector efficiency, ϵ_1, from experiment 003 and the neutron detector efficiency, ϵ_1, from the simulation are shown in the following table. Only statistical errors are given in the table.

Incident Neutron Energy (MeV)	30-40	40-50	50-70
Experiment 003 Data ϵ_1 (%)	6.74±1.81	6.23±1.38	5.74±1.39
Simulation Data ϵ_1 (%)	6.44±0.62	5.96±0.47	5.72±0.41

Table 5.1: The comparison of the neutron detector efficiency, ϵ_1, calculated from experiment 003 data and from the simulation.

The statistical errors in the experiment are poor. This is due to the fact that the running time of experiment 003 was cut short due to a problem with SALAD. According to the Poisson distribution, the standard deviation of *neutrons counted* is $\sqrt{neutron\ counted}$, so the one standard deviation error in the detector efficiency, $\Delta\epsilon_1$, is given by

$$\frac{\Delta\epsilon_1}{\epsilon_1} = \sqrt{\frac{1}{neutron\ counted}}. \tag{5.3}$$

The reasonable agreement, within errors, of the detector efficiency, ϵ_1, between the simulation and the data from experiment 003 confirms the reliability of the simulation code. The good agreement of the response of SALAD, which was discussed in Chapter 4, also attests to the good performance of the simulation code.

With this confidence that the simulation code works, we can then use the simulation to calculate the intrinsic efficiency, ϵ, of the neutron detector. The intrinsic

efficiency cannot be obtained from the experiment 003 data, because we didn't know how many neutrons were deflected from their original direction due to their interaction with SALAD and the SALAD iron cylindrical shield in the experiment.

The intrinsic efficiency, ϵ, of the neutron detector as calculated using the simulation is shown in the following table:

Incident Neutron Energy (MeV)	30-40	40-50	50-70
Simulation Data ϵ (%)	10.72±0.57	10.03±0.45	8.47±0.42

Table 5.2: The neutron detector intrinsic efficiency, ϵ, from the simulation.

The intrinsic efficiency, ϵ, of the neutron detector is consistent with Lennart Isaksson's data [10]. From these data, the intrinsic efficiency of the neutron detector, whose thickness was 10 cm, was about 14% when the incident neutron energy was around 40 MeV.

5.2 Conclusion

So we have confidence in the simulation code. The code can be easily modified to simulate the geometry of any future experiments that use the SAL neutron detector. The SAL neutron detector has been shown to be an effective tool for the detection of neutrons. In fact it was used for a measurement of $^{16}O(\gamma, pn)\ ^{14}N$ cross section at SAL in 1996.

Appendix A
Neutron Time of Flight Calculation Using the Paddle Under SALAD and the SAL Neutron Detector

SALAD and the SAL neutron detector and another timing element arrangement diagram is shown in Figure A.1.

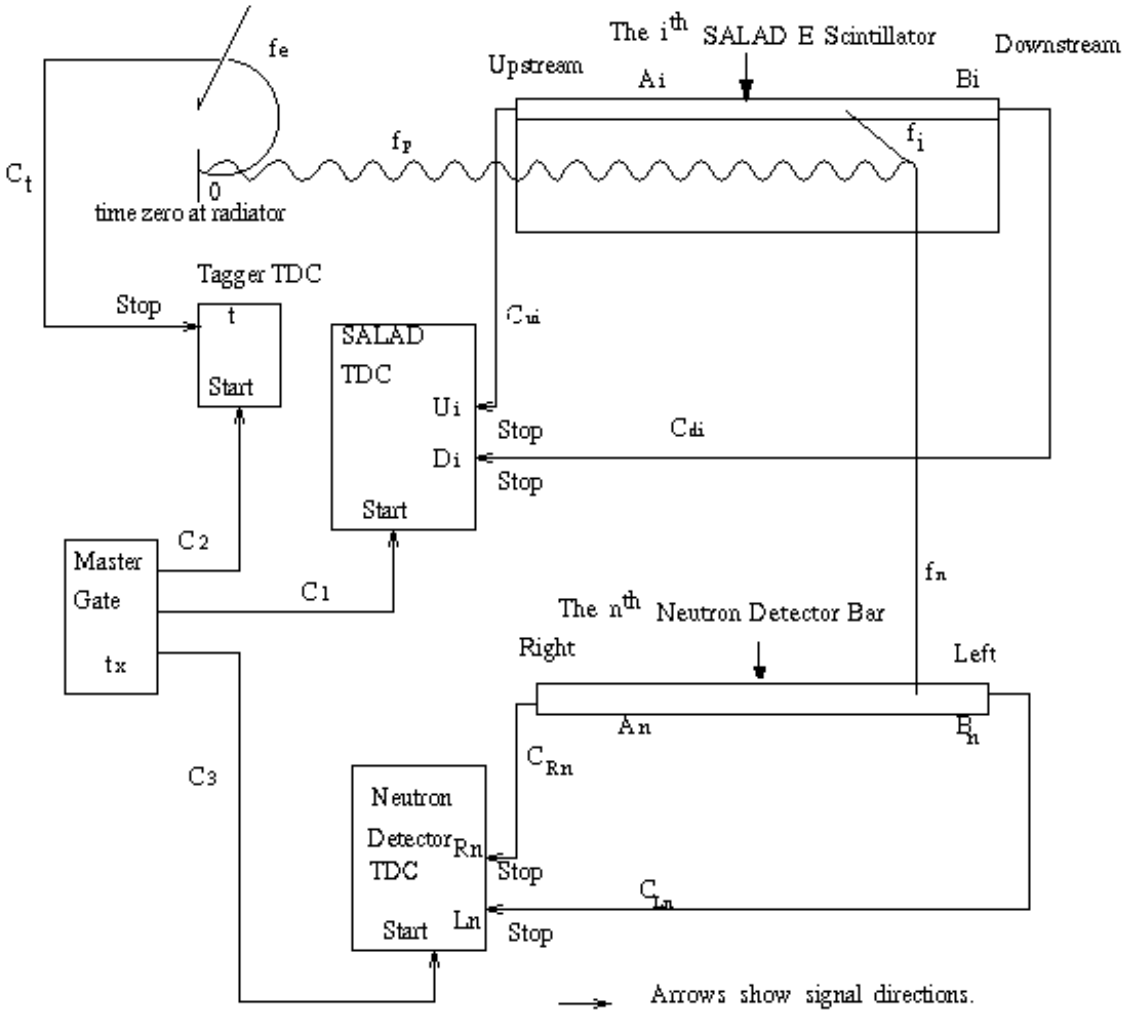

Figure A.1: Timing corrections diagram in experiment 003

Here time zero is the moment that the photon left from the radiator, and
f_e = the post-bremsstrahlung electron flight time from the radiator to the tagger

focal plane.
f_p = the photon flight from the radiator to the target.
f_i = the proton flight time from the target to the SALAD E scintillator.
f_n = the neutron flight time from the target to the neutron detector.
A_i = the light travelling time from the proton hit position in the SALAD E scintillator to the upstream end of the SALAD E scintillator.
B_i = the light travelling time from the proton hit position in the SALAD E scintillator to the downstream end of the SALAD E scintillator.
A_n = the light travelling time from the neutron hit position in the neutron detector to the right end of the neutron detector bar.
B_n = the light travelling time from the neutron hit position in the neutron detector to the left end of the neutron detector bar.
C_{ui} = the signal travelling time from the upstream end of SALAD E scintillator to the SALAD TDC.
C_{di} = the signal travelling time from the downstream end of SALAD E scintillator to the SALAD TDC.
C_{Rn} = the signal travelling time from the right end of the neutron detector bar to the neutron detector TDC.
C_{Ln} = the signal travelling time from the left end of the neutron detector bar to the neutron detector TDC.
U_i, D_i = times measured in SALAD TDC, i.e. stop time - start time in SALAD TDC.
R_n, L_n = times measured in the neutron detector TDC, i.e. stop time - start time in the neutron detector.
C_1 = the signal travelling time from master gate to SALAD TDC.
C_2 = the signal travelling time from master gate to tagger TDC.
C_3 = the signal travelling time from master gate to the neutron detector TDC.
t_x = time of trigger from master gate relative to time zero.
t = times measured in tagger TDC, i.e. stop time - start time in tagger TDC.
For tagger TDC:

$$t = (f_e + C_t) - (t_x + C_2) \tag{A.1}$$

For SALAD TDC:

$$U_i = (f_p + f_i + A_i + C_{ui}) - (t_x + C1) \tag{A.2}$$

$$D_i = (f_p + f_i + B_i + C_{di}) - (t_x + C_1) \tag{A.3}$$

SALAD TDC mean time:

$$t_i = \frac{U_i + D_i}{2}$$

$$= f_p + f_i + \underbrace{\frac{A_i + B_i}{2} + \frac{C_{ui} + C_{di}}{2} - C_1}_{k_i} - t_x \quad \text{(A.4)}$$

In this equation k_i is a constant for each SALAD E scintillator.

For the neutron detector TDC:

$$R_n = (f_p + f_n + A_n + C_{Rn}) - (t_x + C3) \quad \text{(A.5)}$$

$$L_n = (f_p + f_n + B_n + C_{Ln}) - (t_x + C_3) \quad \text{(A.6)}$$

The neutron detector TDC mean time is as follows:

$$\begin{aligned} t_n &= \frac{L_n + R_n}{2} \\ &= f_p + f_n + \underbrace{\frac{A_n + B_n}{2} + \frac{C_{Rn} + C_{Ln}}{2} - C_3}_{k_n} - t_x. \end{aligned} \quad \text{(A.7)}$$

Here k_n is a constant for each neutron detector bar. From equation A.4 and equation A.7, t_x can be cancelled and the neutron time of flight can be obtained:

$$f_n = t_n + f_i - t_i + k_i - k_n. \quad \text{(A.8)}$$

The constants k_i and k_n need to be found.

A timing paddle was put under SALAD to find k_i. The principle is shown in Figure A.2. Time $t = 0$ is the moment that a cosmic muon hit the i^{th} SALAD E scintillator.

f_c = the cosmic muon flight time from the cosmic muon hit position in SALAD E scintillator to the paddle.

C_p = the signal travelling time from the paddle to SALAD TDC.

P_s = times measured in SALAD TDC for the paddle, i.e. stop time - start time in SALAD TDC.

T_x^s = time of trigger from master gate relative to time zero.

From Figure A.2, we know:

$$P_s = (f_c + C_p) - (T_x^s + C_1) \quad \text{(A.9)}$$

$$U_i = (A_i + C_{ui}) - (T_x^s + C_1) \quad \text{(A.10)}$$

$$D_i = (B_i + C_{di}) - (T_x^s + C_1) \quad \text{(A.11)}$$

The mean time of the i^{th} SALAD E scintillator TDC can be obtained from equa-

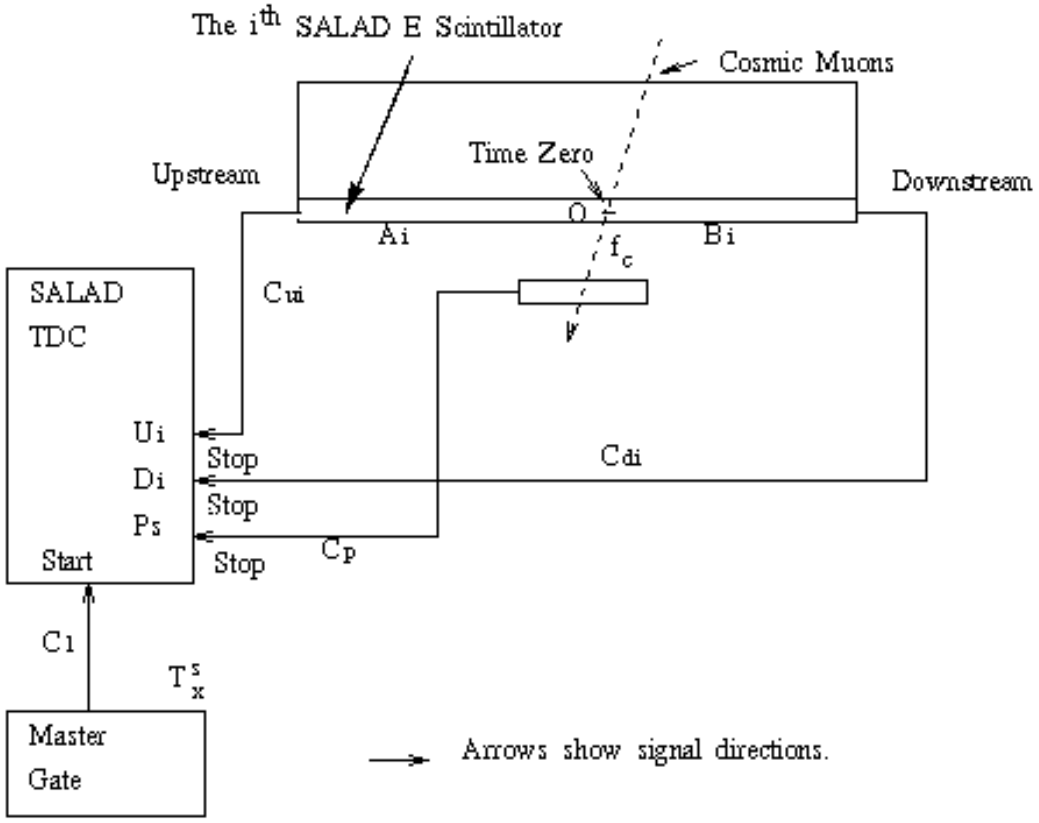

Figure A.2: Timing corrections diagram with a timing paddle under SALAD.

tion A.10 and A.11.

$$\begin{aligned} t_i^s &= \frac{U_i + D_i}{2} \\ &= \underbrace{\frac{A_i + B_i}{2} + \frac{C_{ui} + C_{di}}{2} - C_1}_{k_i} - T_x^s \end{aligned} \tag{A.12}$$

From equation A.9 and equation A.12, T_x^s may be cancelled.

$$k_i = t_i^s + f_c + C_p - C_1 - P_s. \tag{A.13}$$

We define K_i^p as follows:

$$K_i^p = t_i^s + f_p - P_s = k_i - C_p + C_1. \tag{A.14}$$

We can histogram K_i^p, since t_i^s is measured by SALAD TDCs, f_p can be calculated from the muon flight distance assuming the muon speed is near the speed of light, and P_s is measured in SALAD TDC.

The same timing paddle was put under the SAL neutron detector to find k_n. The principle is shown in Figure A.3, Here time $t = 0$ is the moment that the cosmic muon hit the n^{th} neutron detector bar.
f_q = the cosmic muon flight time from the cosmic muon hit position in the n^{th} neutron detector bar to the paddle.
C_p = the signal travelling time from the paddle to SALAD TDC.
P_n = times measured in SALAD TDC for the paddle, i.e. stop time - start time.
T_x^n = time of trigger from master gate relative to time zero.
From Figure A.3, we know:

$$P_n = (f_q + C_p) - (T_x^n + C_1) \tag{A.15}$$

$$R_n = (A_n + C_{Rn}) - (T_x^n + C_3) \tag{A.16}$$

$$L_n = (B_n + C_{Ln}) - (T_x^n + C_3). \tag{A.17}$$

The mean time of neutron n^{th} bar TDC can be obtained from Equation A.16 and A.17.

$$\begin{aligned} t_n^n &= \frac{R_n + L_n}{2} \\ &= \underbrace{\frac{A_n + B_n}{2} + \frac{C_{Rn} + C_{Ln}}{2} - C_3}_{k_n} - T_x^n \end{aligned} \tag{A.18}$$

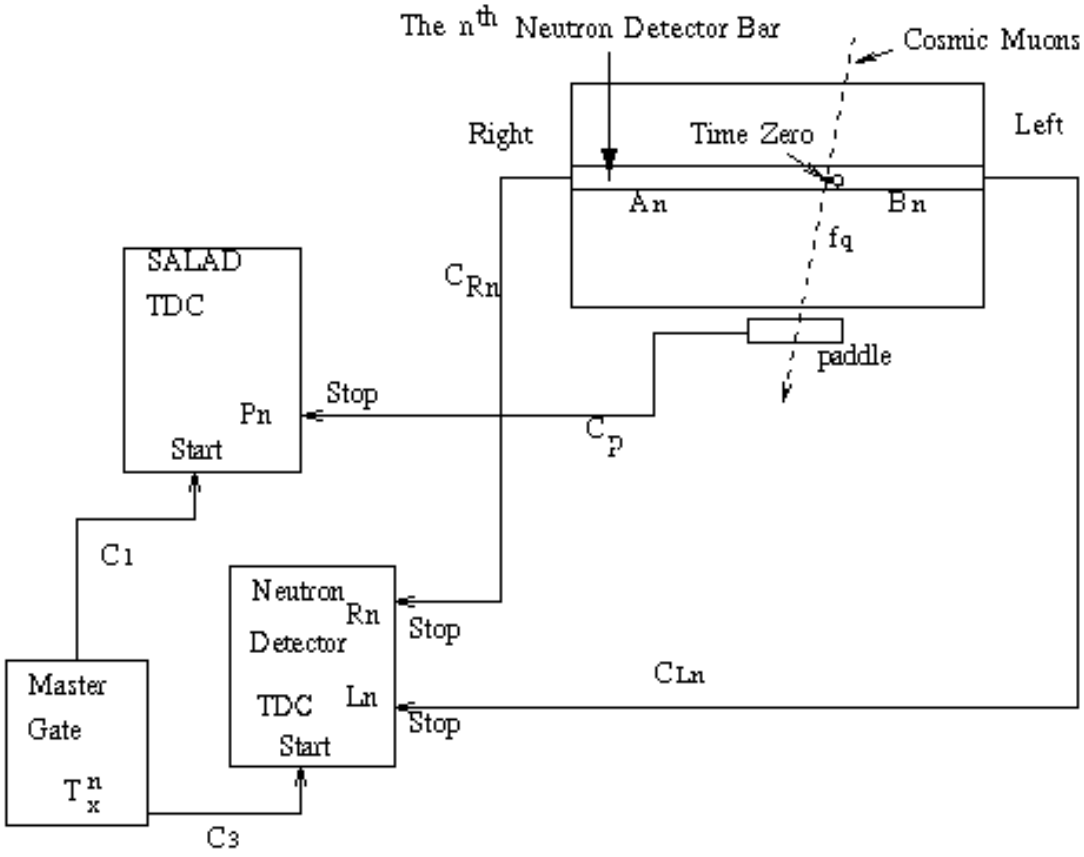

Figure A.3: Timing corrections diagram with a timing paddle under the SAL neutron detector.

From equation A.16 and equation A.18, T_x^n may be cancelled.

$$k_n = t_n^n + f_q + C_p - C_1 - P_n. \tag{A.19}$$

We define K_n^p as follows:

$$K_n^p = t_n^n + f_q - P_n = k_n - C_p + C_1. \tag{A.20}$$

We can histogram K_n^p, since t_n^n is measured by the neutron detector TDCs, f_q can be calculated from the muon flight distance from the neutron detector to the paddle for the muon speed is close to the speed of light, and P_n is measured in SALAD TDC.

From equation A.14 and equation A.20, we can obtain:

$$k_i - k_n = K_i^p - K_n^p. \tag{A.21}$$

If equation A.21 was put into equation A.8, the neutron time of flight can be obtained.

$$f_n = t_n + f_i - t_i + K_i^p - K_n^p. \tag{A.22}$$

Here the constants K_i^p and K_n^p can be found if a timing paddle was put under SALAD and then under the SAL neutron detector.

Appendix B
The Photon Tagger Energy Calibration

The photon energy calibration can be calculated from the electron beam energy and the focal plane central momentum by using the 'tagger_energy' computer program in SAL. Photon tagger energy calibrations can be obtained from the following table.

Table B.1: Photon Tagger Energy Calibration

Standard (62 channel) tagger focal plane.					
Shifted by 0.0 channels, 0.0 mm.				Data: July, 1997	
Electron beam momentum: 252.30 MeV/c				B302: 253.56 MeV/c	
Central tagger momentum (P0): 133.78 MeV/c				Dial: 136.50 MeV/c	
Tagger Field (B0): 0.859 Tesla				Setting number: 377	
Channel Number	Central Momentum (%)	Central Momentum (MeV/c)	Momentum Spread (MeV/c)	Photon Energy (MeV)	Energy Spread (MeV)
1	-17.92	109.80	+/- 0.49	142.50	+/- 0.49
2	-17.18	110.79	+/- 0.50	141.51	+/- 0.50
3	-16.44	111.79	+/- 0.50	140.51	+/- 0.50
4	-15.69	112.79	+/- 0.50	139.51	+/- 0.50
5	-14.94	113.79	+/- 0.50	138.51	+/- 0.50
6	-14.19	114.80	+/- 0.51	137.50	+/- 0.51
7	-13.43	115.82	+/- 0.51	136.48	+/- 0.51
8	-12.67	116.84	+/- 0.51	135.46	+/- 0.51
9	-11.90	117.86	+/- 0.51	134.44	+/- 0.51
10	-11.13	118.89	+/- 0.52	133.41	+/- 0.52
11	-10.36	119.92	+/- 0.52	132.38	+/- 0.52
12	-9.59	120.96	+/- 0.52	131.34	+/- 0.52
13	-8.81	122.00	+/- 0.52	130.30	+/- 0.52
14	-8.02	123.05	+/- 0.52	129.25	+/- 0.52
15	-7.24	124.10	+/- 0.53	128.20	+/- 0.53
16	-6.45	125.16	+/- 0.53	127.14	+/- 0.53
17	-5.65	126.22	+/- 0.53	126.08	+/- 0.53
18	-4.86	127.28	+/- 0.53	125.02	+/- 0.53
19	-4.06	128.36	+/- 0.54	123.94	+/- 0.54
20	-3.25	129.43	+/- 0.54	122.87	+/- 0.54
21	-2.44	130.51	+/- 0.54	121.79	+/- 0.54
22	-1.63	131.60	+/- 0.54	120.70	+/- 0.54
23	-0.82	132.69	+/- 0.55	119.61	+/- 0.55

Table B.2: Photon Tagger Energy Calibration (continue)

Channel Number	Central Momentum (%)	Central Momentum (MeV/c)	Momentum Spread (MeV/c)	Photon Energy (MeV)	Energy Spread (MeV)
24	0.00	133.78	+/- 0.55	118.52	+/- 0.55
25	0.82	134.88	+/- 0.55	117.42	+/- 0.55
26	1.65	135.98	+/- 0.55	116.32	+/- 0.55
27	2.48	137.09	+/- 0.56	115.21	+/- 0.56
28	3.31	138.21	+/- 0.56	114.09	+/- 0.56
29	4.14	139.33	+/- 0.56	112.97	+/- 0.56
30	4.98	140.45	+/- 0.56	111.85	+/- 0.56
31	5.83	141.58	+/- 0.57	110.72	+/- 0.57
32	6.67	142.71	+/- 0.57	109.59	+/- 0.57
33	7.52	143.85	+/- 0.57	108.45	+/- 0.57
34	8.38	144.99	+/- 0.57	107.31	+/- 0.57
35	9.23	146.13	+/- 0.57	106.17	+/- 0.57
36	10.09	147.29	+/- 0.58	105.01	+/- 0.58
37	10.96	148.44	+/- 0.58	103.86	+/- 0.58
38	11.83	149.60	+/- 0.58	102.70	+/- 0.58
39	12.70	150.77	+/- 0.58	101.53	+/- 0.58
40	13.57	151.94	+/- 0.59	100.36	+/- 0.59
41	14.45	153.11	+/- 0.59	99.19	+/- 0.59
42	15.33	154.29	+/- 0.59	98.01	+/- 0.59
43	16.22	155.48	+/- 0.59	96.82	+/- 0.59
44	17.11	156.67	+/- 0.60	95.63	+/- 0.60
45	18.00	157.86	+/- 0.60	94.44	+/- 0.60
46	18.90	159.06	+/- 0.60	93.24	+/- 0.60
47	19.80	160.26	+/- 0.60	92.04	+/- 0.60
48	20.70	161.47	+/- 0.61	90.83	+/- 0.61
49	21.61	162.69	+/- 0.61	89.61	+/- 0.61
50	22.52	163.90	+/- 0.61	88.40	+/- 0.61
51	23.43	165.13	+/- 0.61	87.17	+/- 0.61
52	24.35	166.35	+/- 0.61	85.95	+/- 0.61
53	25.27	167.59	+/- 0.62	84.71	+/- 0.62
54	26.19	168.82	+/- 0.62	83.48	+/- 0.62
55	27.12	170.06	+/- 0.62	82.24	+/- 0.62
56	28.05	171.31	+/- 0.62	80.99	+/- 0.62
57	28.99	172.56	+/- 0.63	79.74	+/- 0.63
58	29.93	173.82	+/- 0.63	78.48	+/- 0.63
59	30.87	175.08	+/- 0.63	77.22	+/- 0.63
60	31.81	176.34	+/- 0.63	75.96	+/- 0.63
61	32.76	177.61	+/- 0.64	74.69	+/- 0.64
62	33.72	178.89	+/- 0.64	73.41	+/- 0.64

References

[1] A.G. Frodesen, O. Skjeggestad and H. Tofte, *Probability and Statistics in Particle Physics.* Universitetsforlaget, Bergen-Oslo-Tromso, 1979

[2] *CERNLIB: CERN Program Library Short Writeups.* Application Software and Databases, Computing and Networks Division, CERN, Geneva, Switzerland, 1994.

[3] E.B. Cairns, J.Cameron, etc. *The Saskatchewan-Alberta large acceptance detector for photonuclear physics.* Nuclear Instruments and Methods in Physics Research A 321 (1992) 109-118

[4] Evan David Joseph Hackett *Multi-proton Emission in Photon Induced Reactions on* ^{12}C Ph.D. thesis. University of Albert, Edmonton, 1995

[5] *GEANT User's Guide.* Application Software and Databases, Computing and Networks Division, CERN, Geneva, Switzerland, 1991.

[6] G.V. O'Rielly, N.R.Kolb and R.E. Pywell *The Response of Plastic Scintillator to Protons and Deuterons.* Nuclear Instruments and Methods in Physics Research A 368 (1996) 745-749

[7] J.B. Marion and F.C. Young, *Nuclear Reaction Analysis.* North-Holland, Amsterdam, 1968.

[8] John M. Blatt and Victor F. Weisskopf, *Theoretical Nuclear Physics.* Dover Publications, Inc, New York, 1991

[9] Keith Helgi Jacob Helgason, *A Large-Area Neutron Detector* M.Sc. thesis. University of Saskatchewan, Saskatoon, Spring, 1995

[10] Lenart Isaksson, *High-Resolution Measurement of the* $^{16}O(\gamma, pn)$ *Reaction.* Lund, Sweden 1996.

[11] *PAW: Physics Analysis Workstation the Complete Reference.* Application Software Group, Computing and Networks Division, CERN, Geneva, Switzerland, 1989.

[12] Philip Patrick Langill *A Large Acceptance Detector for Photonuclear Reactions* M.Sc. thesis. University of Albert, Edmonton, Fall, 1989

[13] W.R. Leo, *Techniques for Nuclear and Particle Physics Experiments.* Springer-Verlag, Berlin Heidelberg, 1987.